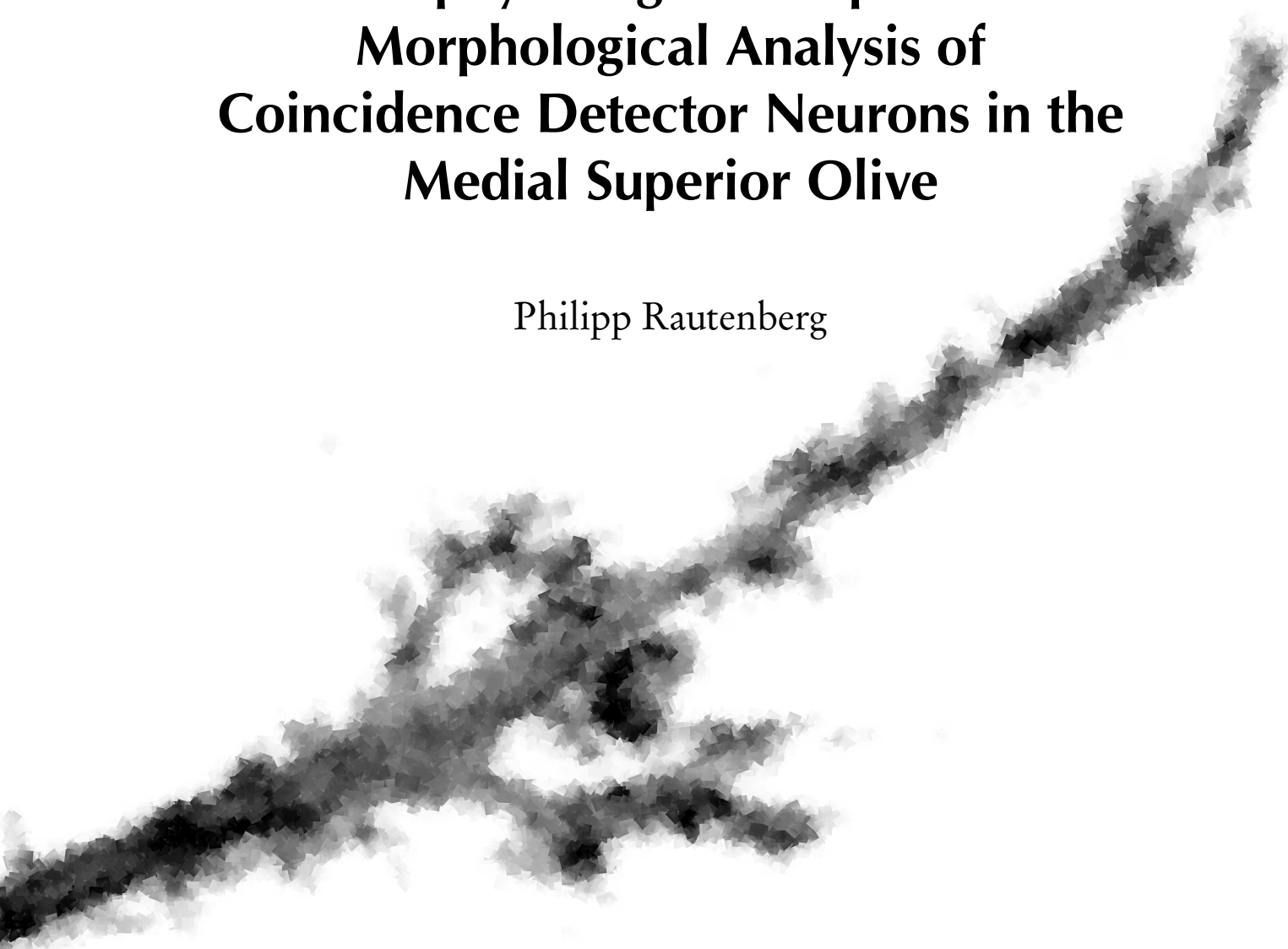


Dissertation

**Developmental Alterations and
Electrophysiological Properties: a
Morphological Analysis of
Coincidence Detector Neurons in the
Medial Superior Olive**

Philipp Rautenberg



Developmental Alterations and Electrophysiological Properties: a Morphological
Analysis of Coincidence Detector Neurons in the Medial Superior Olive

Dissertation

**Developmental Alterations and
Electrophysiological Properties: A
Morphological Analysis of
Coincidence Detector Neurons in the
Medial Superior Olive**

Philipp Rautenberg

2011



Graduate School of Systemic Neurosciences
Ludwig-Maximilians-Universität München

Supported by Bundesministerium für Bildung und Forschung through the
Bernstein Center for Computational Neuroscience (BCCN), München
Grant number: 01GQ0440

Supervisors:
Prof. Dr. Benedikt Grothe
Prof. Dr. Christian Leibold
Tag der mündlichen Prüfung: 30. März 2012

Meiner Familie –
besonders meinen Eltern,
die immer für mich da sind,
wenn ich sie brauche!

Preface

Summary

The medial superior olive (MSO) is an auditory brainstem nucleus within the superior olivary complex. Its functional role for sound source localization has been thoroughly investigated (for review see Grothe et al., 2010). However, few quantitative data about the morphology of these neuronal coincidence detectors are available and computational models incorporating detailed reconstructions do not exist. This leaves open questions about metric characteristics of the morphology of MSO neurons as well as about electrophysiological properties that can be discovered using detailed multicompartmental models: what are the passive parameters of the membrane? What is the axial resistivity? How do dendrites integrate synaptic events? Is the medial dendrite symmetric to the lateral dendrite with respect to integration of synaptic events?

This thesis has two main aspects: on the one hand, I examined the shape of a MSO neuron by developing and applying various morphological quantifications. On the other hand, I looked at the impact of morphology on basic electrophysiological properties and on characteristics of coincidence detection. As animal model I used Mongolian gerbils (*Meriones unguiculatus*) during the late phase of development between postnatal day 9 (P9) and 37 (P37). This period of time is of special interest, as it spans from just before hearing onset at P12 – P13 (Finck et al., 1972; Ryan et al., 1982; Smith and Kraus, 1987) to adulthood. I used single cell electroporation, microscopic reconstruction, and compartmentalization to extract anatomical parameters

of MSO neurons, to quantitatively describe their morphology and development, and to establish multi-compartmental models.

I found that maturation of the morphology is completed around P27, when the MSO neurons are morphologically compact and cylinder-like. Dendritic arbors become less complex between P9 and P21 as the number of branch points, the total cell length, and the amount of cell membrane decrease. Dendritic radius increases until P27 and is likely to be the main source of the increase in cell volume. In addition, I showed that in more than 85% of all MSO neurons, the axonal origin is located at the soma.

I estimated the axial resistivity ($80 \Omega \cdot \text{cm}$) and the development of the resting conductance (total conductance during the state of resting potential) which reaches $3 \text{ mS}/\text{cm}^2$ in adult gerbils. Applying these parameters, multi-compartmental models showed that medial versus lateral dendritic trees do not equally integrate comparable synaptic inputs. On average, latencies to peak and rise times of lateral stimulation are longer ($12 \mu\text{s}$ and $5 \mu\text{s}$, respectively) compared to medial stimulation. This is reflected in the fact that volume, surface area, and total cell length of the lateral dendritic trees are significantly more larger in comparison to the medial ones.

Simplified models of MSO neurons showed that dendrites improve coincidence detection (Agmon-Snir et al., 1998; Grau-Serrat et al., 2003; Dasika et al., 2007). Here, I confirmed these findings also for multi-compartmental models with biological realistic morphologies. However, the improvement of coincidence detection by dendrites decreases during early postnatal development.

Remarks

All data presented in this thesis was collected and analyzed by myself with support of my supervisors. In the lab, I established necessary methods for morphological 3D-reconstruction and multicompartmental modeling. As this effort engaged intensive work and resulted in fruitful discussion within the lab as well as on various

conferences, I decided to discuss also methodological aspects within the last chapter 5.2.

Part of the present work has been published in Rautenberg et al., 2009. This concerns mainly the metric quantification of the morphology of MSO neurons.

Contents

Preface	7
1 Introduction	13
1.1 Psychophysical Motivation	13
1.2 Computational principles	14
1.3 Anatomy of the Auditory Brainstem and Pathways for Spatial Processing	14
1.4 Processing of Continuous Sound Signals for Sound Localization – From the Cochlear Nucleus to the MSO	15
1.5 Intracellular ITD Processing – Dealing With the Lack of Delay Lines (in Mammals)	18
1.6 Properties of Neurons of the Medial Superior Olive	19
1.6.1 Morphological development of MSO-neurons	19
1.6.2 Multi-Compartmental Models of the MSO	21
2 Materials & Methods	25
2.1 Slice Preparation	25
2.2 Electroporation	25
2.3 Cell Reconstruction	26
2.4 Tissue Alterations Imposed by the Experimental Procedure	28
2.5 Multi-Compartmental Modeling	29
3 Quantification of the Three-Dimensional Morphology	31
3.1 Somatic Architecture of MSO Neurons	31

3.2	Axonal Origin of MSO Neurons	33
3.3	Developmental Changes in the Dendritic Arborization Pattern	33
3.4	Quantification of the Overall MSO Cell Architecture	35
3.5	Metric Criterion of Filopodia	39
3.6	Distribution of Surface Area and its Development	41
4	Electrophysiological Properties, Symmetry, and Coincidence-Detection-Characteristics of MSO Morphologies	45
4.1	Influence of Passive Conductance and Axial Resistivity on Input Resistance and Effective Membrane Time Constant	46
4.2	Estimation of Axial Resistivity	49
4.3	Estimation of Passive Conductance	53
4.4	Correlating Electrophysiological with Metric Properties	55
4.5	Asymmetry of MSO-Neurons	56
4.6	Coincidence Detection	61
5	Discussion	65
5.1	New Findings on Properties of Neurons of the MSO	66
5.1.1	MSO-Morphologies Improve Coincidence Detection	66
5.1.2	Development of MSO-Morphologies After Hearing Onset	67
5.1.3	Estimating Passive Parameters of Models of MSO neurons	68
5.1.4	The Influences of Activity on MSO-Morphologies	69
5.1.5	Morphological Assymetries and its Implications	70
5.2	Widening the View: Implications on Other Areas	72
5.2.1	Transformation of Brain Tissue Modifies the Neurons Shape During Methodolocial Procedures	72
5.2.2	Reducing Complexity of Detailed Multi-Compartmental Models and Mapping Functions Onto Neuronal Morphology	73
5.2.3	Morphologies Implement Divers Arborization Patterns	74
5.3	Conclusion	76

6 Appendix	77
6.1 Timeline	79
Bibliography	81
Epilogue	93

List of Figures

1.1	Sound Localization and Processing Brain Structures	16
3.1	Somatic Morphology of Individually Labeled Neurons of the Medial Superior Olive	32
3.2	Pattern of Dendritic Arborization	34
3.3	Kleine Statistik	37
3.4	Maturation of Dendritic Thickness	38
3.5	Dendritic Appendages	40
3.6	Surface Area Distribution	42
4.1	Illustration of Electrophysiological Simulation	46
4.2	Input Resistance and Effective Time Constant for Varying Parameters	48
4.3	Fitting Axial Resistivity and Passive Conductance to Individual Combinations of Input Resistance and Time Constant.	50
4.4	Distribution of Specific Resistivity and Passive Conductance for Equally Distributed Input Resistance	51
4.5	Estimation of the Axial Resistivity With Asymptotic Values for Input Resistance and Effective Membrane Time Constant	52
4.6	Modulation Indices and Estimation of Passive Conductance	54
4.7	Correlation Between Metric and Electrophysiological Properties	55
4.8	Morphological Symmetry	57
4.9	Electrophysiological Symmetry	59
4.10	Development of Electrophysiological Properties	60
4.11	Illustration of the Paradigm of Coincidence Detection	61

List of Figures

4.12 Coincidence-Detection-Characteristics 63

1 Introduction

1.1 Psychophysical Motivation

Imagine the following situation: you are sitting at your desk writing your PhD-thesis. Suddenly the cell phone rings. Without even looking you grasp – and hold the cell phone in your hand. But how did you solve this rather difficult task? Our brain uses several cues in order to solve this challenge. One of them is the time difference at which the sound arrives at our two ears: if somebody is standing left of you calling your name, his spoken words will arrive first at the left ear and after a tiny delay – the interaural time difference (ITD) – at the right one (Fig. 1.1A). This ITD-cue together with other ones¹ allows our brain to estimate the location of a sound source in 3D-space. Especially for localization in the horizontal plane, ITD of low frequencies serves as the most important cue (Wightman and Kistler, 1992). Thresholds for the detection of ITD are of an order of ten millionth of a second for mammals (Klumpp and Eady, 1956). With this magnitude in time, sound localization can be considered to have one of the fastest underlying processes in the brain. Evolution developed highly specialized neurons within the brain to calculate this time difference. These neurons get input from both ears and, therefore, are able to compare the arrival time at each ear of one sound signal. Their coding is just

¹From a pure physical point of view and just relying on time differences as physical cues, 3D-localization of a sinusoidal sound would need four ears (not just three!) that are arranged in space like the corners of a tetrahedron (not necessarily a tetrahedron with four equilateral triangles). As we have just two ears, we need more cues for precise sound localization in 3D-space. These other cues are for instance the interaural level difference of a sound at both ears, or the frequency filtering by the pinna (Thompson, 1882; Rayleigh, 1907; Coleman, 1963; Batteau, 1967). For review see Middlebrooks and Green, 1991).

one component of neuronal processing on the way to higher cortical areas. At the stage of conscious cognition, we don't experience the doubly received signal as two distinct and temporally displaced sound objects (like an original sound and its echo) but as one, originating at a specific position in space. This is how you immediately know the location of your ringing cell phone!

1.2 Computational principles

Within the brain, neurons assemble diverse circuits that implement specific computational principles like winner-takes-it-all-networks, lateral inhibition, or coincidence detection. Each computational principle serves different tasks. Coincidence detection – a process that is subject of the present thesis – plays a crucial role e.g. for long-term potentiation at pyramidal cells (Hebb's rule “cells that fire together, wire together”), but also for processing sound localization at the brainstem. Here, cells from the medial superior olive use coincidence detection for calculating ITDs.

1.3 Anatomy of the Auditory Brainstem and Pathways for Spatial Processing

Within the cochlea, sound is transformed from a pressure wave representation to a neural representation: Mechano-electrical transduction channels of hair cells are coupled to auditory stimuli. As a consequence, the mechanical properties of these channels shape our hearing process from the outset of signal transduction (Hudspeth et al., 2000). Mechanically coupled ion channels in the stereocilia² of hair cells are very rapidly opened and closed in synchrony with the displacement of the basilar membrane. Single auditory nerve fiber discharges are able to follow these channel openings, or *phase-lock*, to frequencies up to 4 kHz in mammals (Moore et al., 2001; Trussell, 1999). As part of the nervus vestibulocochlearis (the 8th cranial nerve),

²Stereocilium is the “hair” of a hair cell and has a size of $< 1 \mu\text{m}$ to $> 300 \mu\text{m}$ in length (Hudspeth et al., 2000).

the auditory nerve (AN) receives its input from hair cells. The AN transmits the underlying acoustic information to different target neurons in the cochlear nucleus (CN) (Ryugo and Parks, 2003).

The CN is the first stage in the auditory brainstem. The auditory brainstem covers additionally the following main structures: the superior olivary complex (SOC) and the nuclei of the lateral lemniscus. Within the auditory brainstem, the ventral cochlear nucleus (VCN) along with the spherical bushy cells (SBC) and globular bushy cells (GBC), the medial nucleus of trapezoid body (MNTB), the lateral nucleus of the trapezoid body (LNTB), and the medial superior olive (MSO) build a circuit for ITDs processing (Fig. 1.1B). SBCs project excitatory input directly to MSO neurons. GBCs project excitatory input to neurons of the ipsilateral LNTB and the contralateral MNTB, which project both to the MSO with inhibitory synapses (Adams and Mugnaini, 1990). Here, at the MSO, a central processing of ITD information takes place and the output is then relayed via the inferior colliculus and lateral lemniscus to the higher cortical areas (Adams, 1979; Nordeen et al., 1983; Moore and Kitzes, 1985; Shneiderman et al., 1988).

1.4 Processing of Continuous Sound Signals for Sound Localization – From the Cochlear Nucleus to the MSO

The neuronal circuit for ITD processing represent one of the fastest neural systems in the human brain. Its information processing is based on sub-millisecond spike timing. The minimal ITD that humans can resolve is in a range of $10 \mu\text{s}$ (Klumpp and Eady, 1956). Specialized structural properties are necessary to allow successful processing and encoding of these ITDs in order to acquire this temporal resolution. Therefore, ITD-processing structures form an appropriate system to investigate and to disentangle mechanisms underlying precise temporal processing in the vertebrate brain, and have already encouraged many experimental studies and computational

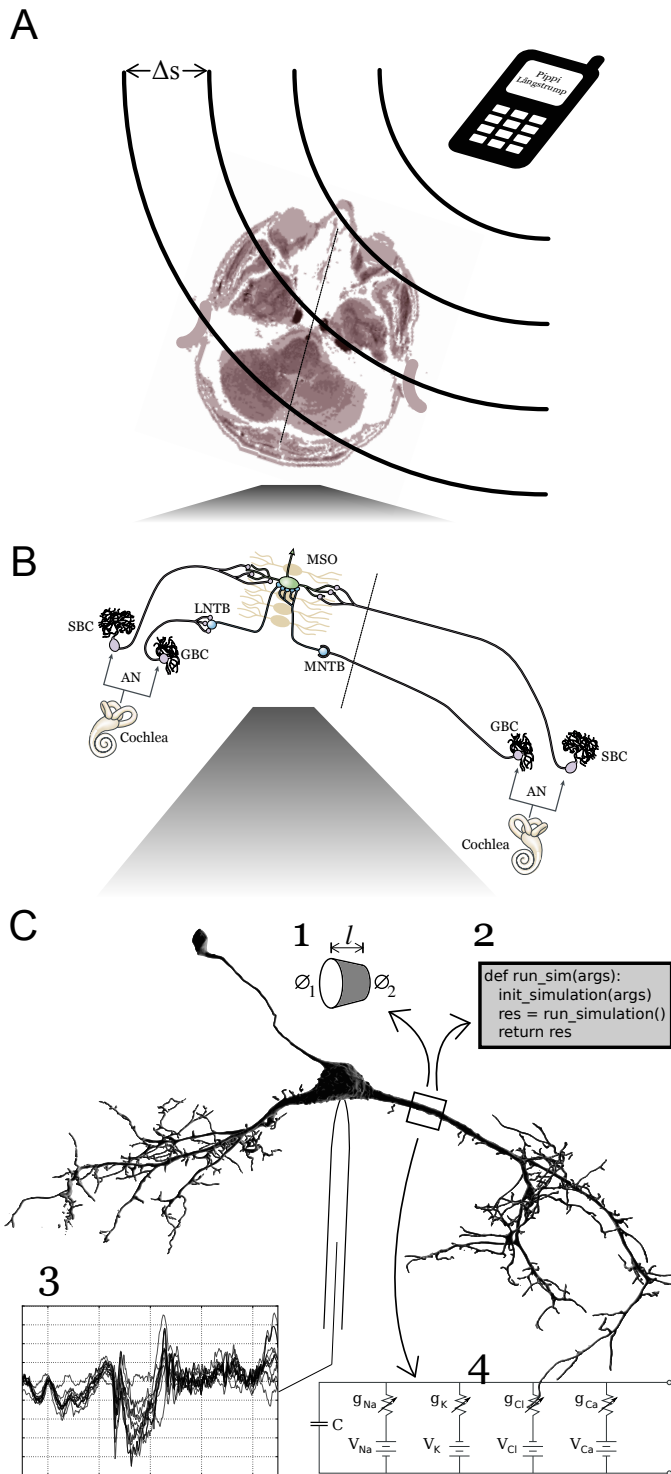


Figure 1.1: Sound localization and processing brain structures. **A:** The sound of the ringing cell phone arrives first at the right ear and after a tiny delay – the interaural time difference (ITD) – at the left ear. Here the ITD $\Delta t = \Delta s/c$ (with $c =$ speed of sound and $\Delta s =$ difference in distance to the sound source to each ear). For low frequencies of a sound wave (< 4 kHz), this cue allows our brain to estimate the location of a sound source in the horizontal plain. **B:** (Modified from Grothe 2003, Fig. 4a) The auditory nerve transmits environmental acoustic information to various target neurons of spherical bushy cells (SBC) and globular bushy cells (GBC). SBCs give excitatory input to medial superior olive (MSO) neurons. GBCs give excitatory input to neurons of the ipsilateral lateral nucleus of the trapezoid body (LNTB) and the contralateral medial nucleus of trapezoid body which project both to the MSO with inhibitory synapses. The morphology of cells in the MSO has bipolar shape with an orientation that is mainly perpendicular to the dorsoventral main plain. The resulting plain segregates different synaptic inputs on MSO neurons anatomically. **C:** This sketch illustrates applications of morphological reconstructions with a reconstructed MSO neuron of a ten postnatal days old gerbil. Analysis functions approximate morphologies by many frusta (1) in order to calculate properties like surface area and volume of a neuron. Scripts (2) initialize simulators like NEURON with according morphological information and parameters to simulate for instance an electrophysiological patch clamp experiment (3). These simulators make use of the fact that membrane properties which are responsible for the electric potential of neurons can be described by electric circuits (4).

models (McAlpine and Grothe, 2003; Pecka et al., 2007; Dasika et al., 2007; Grothe et al., 2010).

Auditory signals arrive at the cochlea as waveforms that are continuous in time and not discrete events and thus hamper its ability to compare arrival times³. In order to reference to discrete points in time of a given analog waveform, neurons respond to specific phases of the signal. Here, the timing accuracy of this response can be quantified as vector strength⁴ (Goldberg and Brown, 1969). Interestingly, vector strength improves at neurons on the pathway to the MSO, e.g. for pure tones at the bushy cells (Smith et al., 1991; Joris and Smith, 2008). In order to accomplish this, one mechanism is (monaural) coincidence detection of different spikes converging several inputs into a single output. Here, the output is more precise in terms of vector strength than the input (Covey and Casseday, 1991; Reed et al., 2002).

Within the mentioned auditory circuit, the MSO is the first nucleus which processes binaural inputs. Its morphology, its membrane with active and passive channels, and its intracellular resistivity influence transforming inhibitory and excitatory inputs – each originating from either of the ears – into a neuronal signal coding ITDs. It uses the temporal correlation between those excitatory and inhibitory inputs to process ITD, allowing the localization of low-frequency sounds in the azimuthal plane (Goldberg and Brown, 1969; Yin and Chan, 1990).

³For ITD processing, the order of magnitude of the information is in the same range as the order of magnitude of the underlying physical carrier (one wave length of a 2 kHz tone lasts for 500 μ s). *When a man speaks, the wave length of the sounds he produces is perhaps eight feet, and it is evident we could not carry about with us any kind of lens which would be many multiples of eight feet; in fact, the human body is not big enough to do for sound anything like the same thing as the eye does for light. One must look therefore for the explanation for the possibility of telling in what direction a sound is, in an entirely different quarter* (Rayleigh, 1876).

⁴Vector strength of zero: spikes take place randomly distributed with respect to phase; vector strength of one: spikes take place exactly at the same phase

1.5 Intracellular ITD Processing – Dealing With the Lack of Delay Lines (in Mammals)

In theory, varying delay lines of excitatory inputs from each ear could exactly compensate specific ITDs. Based on this assumption, the problem of discriminating ITDs can be solved by detection of coinciding inputs: an array of coincidence detectors with varying delay lines would transform ITDs into a place code and by this establish a map of ITDs (Jeffress, 1948). Axons with different length would serve as delay lines. Carr and Konishi (1990) showed that axonal delay lines form maps of ITD in the nucleus laminaris (NL, the avian homologue of the MSO) of the barn owl (Köppl and Carr, 2008). Together with other studies (Grothe et al., 2004; Kubke et al., 2004; MacLeod et al., 2006) they showed that these delay lines are the plesiomorphic pattern in birds.

In the mammalian system no clear anatomical evidence of comparable delay line structures has been reported (Smith et al., 1993; Beckius et al., 1999). Increasingly conflicting findings began to challenge the validity of the *Jeffress model* for the MSO, the mammalian ITD detector (Brand et al., 2002; Grothe, 2003; McAlpine et al., 2001). Brand et al. (2002) showed that a map of ITDs – as it would be implied by the *Jeffress model* – does not exist. Moreover, they showed that glycinergic inhibition affects the tuning of a neuron for ITD significantly (McAlpine and Grothe, 2003; Pecka et al., 2008).

In order to better understand ITD processing – that is based on excitatory and inhibitory inputs – I focussed in my thesis on cellular properties of MSO neurons of gerbils, a well-established animal model of sound localization (like humans, gerbils use ITDs to localize low frequencies below 1500 Hz). I investigated the morphological characteristics starting with a metric quantification of MSO neurons and, then, I established a multicompartamental model to investigate basic electrophysiological properties.

1.6 Properties of Neurons of the Medial Superior Olive

Neurons of the MSO process binaural information. This fact is reflected by the shape of the cells as well as the arrangement of the nucleus. The most prominent property of the morphology of cells in the MSO is the bipolar shape with an orientation that is mainly perpendicular to the dorsoventral main plain of the nucleus (Cajal, 1909; Stotler, 1953; Kiss and Majorossy, 1983; Henkel and Brunso-bechtold, 1990; Kulesza, 2007). This plain segregates excitatory synaptic inputs on MSO neurons anatomically (Fig. 1.1B). MSO neurons receive excitatory input mainly on dendrites and inhibitory inputs on the somatic region (Stotler, 1953; Clark, 1969; Adams and Mugnaini, 1990; Kuwabara and Zook, 1992; Kapfer et al., 2002). Excitatory input at lateral dendrites originates from neurons that respond to ipsilateral stimulation. Excitatory input at medial dendrites originate from neurons that respond to contralateral stimulation. Therefore, the bipolarity of the MSO neurons segregates the excitatory inputs to a given dendrite according to the site of its origin, respectively (Stotler, 1953).

In my thesis, I investigated the shape of MSO-cells and its development: Where do axons originate from? What is the time-course of dendritic development with respect to basic measures like surface area, volume? In addition, I simulated electrophysiological models of MSO-cells to estimate passive parameters and to explore the morphological contribution to dendritic symmetry of signal processing and to coincidence detection.

1.6.1 Morphological development of MSO-neurons

The type of a neuron's morphology influences the signal processing that is accomplished by that neuron. A detailed 3D-quantification of the changes in the overall cellular morphology of mammalian MSO neurons during late development through adulthood is the first part of my thesis (chapter 3).

Dendrites of neurons in the MSO of adult albino rats are low in complexity, with a tube-like appearance (Feng and Rogowski, 1980) similar to neurons in the avian

analog structure, the nucleus laminaris (NL; Smith, 1981; Wang and Rubel, 2008). Neurons of the superior olivary complex (SOC) in mammals undergo morphological changes during development in gerbils, rats, and ferrets (Rogowski and Feng, 1981; Sanes et al., 1992a; Rietzel and Friauf, 1998; Chirila et al., 2007). In the MSO and the lateral superior olive (LSO), the dendritic arbor and the total cell length become reduced during postnatal development in rats and gerbils (Rogowski and Feng, 1981; Sanes et al., 1992a; Rietzel and Friauf, 1998; Chirila et al., 2007). In neurons of the gerbil MSO, small cellular protrusions appear to be retracted by P12 (Chirila et al., 2007).

Hearing onset in gerbils occurs at P12–P13 (Finck et al., 1972; Ryan et al., 1982; Smith and Kraus, 1987). From this time on, cellular mechanisms that are dependent on neuronal activity driven by acoustic stimuli might control cellular anatomy within the auditory circuits. It has been demonstrated that activity-dependent refinement occurs in the auditory brainstem of mammals (Stotler, 1953; Kiss and Majorosy, 1983; Sanes et al., 1990, 1992a; Rietzel and Friauf, 1998; Magnusson et al., 2005; Werthat et al., 2008). In the LSO, the extent of dendritic arborization appears to correlate with position along the tonotopic gradient (Sanes et al., 1990), and its refinement is affected by auditory deprivation (Sanes et al., 1992a). Developmental activity-dependent refinement was also shown for the MSO of albino rats (Feng and Rogowski, 1980) and the avian analog, the NL, of chickens (Wang and Rubel, 2008). These studies suggest that cellular refinement continues after hearing onset in an activity-dependent manner. However, no quantification of the developmental alterations based on metric values is available for MSO neurons in the gerbil. Such quantification is also of importance to estimate how activity-dependent processes affect different parameters of the cell morphology, such as cell volume, cell surface, and dendritic length.

The quantification of subcellular structures of cells in the mammalian MSO is also important from a comparative point of view, as it allows comparison to the brain structure found in auditory pathways of the avian brainstem. There, the NL integrates binaural synaptic inputs and codes for ITDs (Carr and Konishi, 1990; Overholt et al., 1992; Köppl and Carr, 2008). The morphology and the development of cells

and their dendrites in the NL has been quantified (Smith, 1981). Similar to neurons in the MSO, neurons in the NL are arranged in a bipolar fashion (Smith, 1981; Wang and Rubel, 2008). The ipsilateral and contralateral excitatory inputs to NL neurons are segregated to the different dendrites. It was inferred from computer simulations that cellular arrangement in the NL has functional implications in generating the temporally precise postsynaptic integration that underlies binaural coincidence detection (Agmon-Snir et al., 1998; Grau-Serrat et al., 2003; Dasika et al., 2007). A morphological description of neurons in the mammalian MSO would allow for an anatomical and functional comparative analysis. As it seems that neural implementation for ITD is different between birds and mammals at the level of the circuitry, differences on a cellular level will be relevant for understanding ITD processing.

In particular, cellular morphology – especially the dendritic architecture – turns out to be of functional significance to post-synaptic integration mechanisms and certainly subject to developmental refinement (Cuntz et al., 2007). First observations show that principal MSO neurons are mainly bipolar (Grothe, 2003) and that the axon primarily emerges from the soma (Scott et al., 2005).

Morphology of MSO neurons in gerbils and their developmental alterations between P9 and P36 were quantified in the present thesis. The examined developmental period spans the transition from before hearing onset to adulthood. I provide quantitative evidence that cellular shaping occurs until P27, indicating that developmental changes could be affected by sensory stimulation as hearing onset occurs at P12 – P13 (Finck et al., 1972; Ryan et al., 1982; Smith and Kraus, 1987). Furthermore, I could show that the developmental cellular shaping leads to an anatomically compact, cylinder-like morphology.

1.6.2 Multi-Compartmental Models of the MSO

Neurons typically have elaborate and distinctive dendritic trees that receive synaptic input. The integration of this synaptic input depends on many different properties like axial resistivity, passive membrane conductance, active channels and their distribution across the membrane, and the structure of the dendritic tree itself.

Many attempts to examine the influence of dendrites on synaptic integration are based on mathematical representations of dendrites and their electrical properties (Rall, 1959, 1964; Gullledge et al., 2005). Certain experiments that obtain their results with intracellular electrodes require a theory which treats the spread of current within branching dendritic trees (Rall, 1959). Such theories approximate dendrites by electrical cables and, therefore, are able to use existing equations that describe signal propagation in submarine telegraph cables.

In addition to a neuron's shape, modeling the passive properties of its membrane requires a knowledge of the specific membrane conductance (g_m), the specific membrane capacity (c_m), and the axial resistivity (ρ) (Fig. 1.1C). In combination with the morphology of a neuron, these parameters influence the characteristics of the impact of synaptic events within passive dendrites, for instance, time constants and electrotonic length of membrane cylinders and neurons (Rall, 1969):

$$c_m \cdot \frac{\partial V(x)}{\partial t} = \frac{r}{2\rho} \cdot \frac{\partial^2 V(x)}{(\partial x)^2} - g_m V(x) \quad (1.1)$$

Differences in the morphologies are related to functional differences (Rall, 1995; Mainen and Sejnowski, 1996; Vetter et al., 2001; Stiefel and Sejnowski, 2007). Firing rates and bursting duration are regarded as parameters for information representation (Krichmar et al., 2002; Decharms and Zador, 2000; Bialek and Zee, 1990). Morphology has been shown to influence these parameters (Larkman and Mason, 1990; Mason and Larkman, 1990).

Across the nervous system, neurons possess a variety of dendritic morphology. Within the auditory circuit that I described above are two exemplary functions which are supported by the dendritic structure of the corresponding neurons: monaural coincidence detection by GBCs and binaural coincidence by cell of the MSO. The dendritic trees of these two types of neurons can be distinguished by clear characteristics: typical GBCs have one primary dendrite that branches into many subtrees that receive excitatory input from different AN fibers originating from the ipsilateral cochlea. By processing coinciding synaptic events, GBCs increase the vector

strength of its output compared to its input. In contrast, primary neurons of the MSO have two primary dendrites that also branch into subtrees. Here, one role is the segregation of ipsilateral and contralateral inputs as described above. Another role is to support coincidence detection. Postsynaptic integration by the lateral and medial dendrites may be involved in generating the sub-millisecond precision of coincidence detection (Agmon-Snir et al., 1998; Grau-Serrat et al., 2003; Dasika et al., 2007)). Parameters of dendritic anatomy, such as diameter and extent of arborization, influence postsynaptic integration mechanisms (Rall et al., 1992; Mainen and Sejnowski, 1996).

The fact that delay lines do not exist in the mammalian brainstem leads to new questions as well as to new computational models. Here, some models concentrate exclusively on coincidence detection from two excitatory inputs (Agmon-Snir et al., 1998). Other models try to explain the ITD shift via inhibitory inputs, like the asymmetrical cell model (Zhou et al., 2005), assuming an asymmetrical axonal placement that was computationally demonstrated to influence coincidence detection.⁵

In the second part of my thesis (chapter 4), I used the reconstructed morphologies for further analysis via multi-compartmental models. With these multi-compartmental models I estimated reasonable passive parameters of MSO neurons. Based on these parameters I analyzed the correlation between metric and electrophysiological properties of morphologies of the MSO. In addition, I investigated the explicit morphological influence on symmetric processing of synaptic input and coincidence detection with respect to electrophysiological measurements.

⁵The implementation of the corresponding model contains a dubious implementation of the Sodium (na) channel. The file `na_VCN2003.mod` comments the na-definition correctly (line 3, `na=gna*m^3*h`) corresponding to the referred paper (Rothman and Manis, 2003). But the implementation later does not correspond to that (line 61, `gna=gnabar * m*m*h`, which implements not m^3 but m^2 which corresponds to data from Rothman and Young, 1996). However, debugging this error and adjusting some parameters the results of the publication could be confirmed (from private conversation and data exchange with Yi Zhou).

2 Materials & Methods

Viva la convolución!

(Álvaro Tejero-Cantero)

2.1 Slice Preparation

All experiments complied with institutional guidelines, and with national and regional laws. Animals were sacrificed by decapitation and brains were rapidly removed in dissecting solution. The dissection solution for gerbils younger than P18 was ice cold, and contained (in mM) 125 NaCl, 25 NaHCO₃, 2.5 KCl, 1.25 NaH₂PO₄, 3 MgCl₂, 0.1 CaCl₂, 25 glucose, 0.4 ascorbic acid, 3 myo-inositol, and 2 Na-pyruvate (pH 7.4 when bubbled with 95% O₂ and 5% CO₂). For dissecting gerbils older than P18, the solution was prewarmed, and sodium was partially substituted with 48 mM sucrose, yielding a final concentration of 25 mM NaCl. After dissection, transverse brainstem slices containing the medial superior olive (MSO) were taken from 9 – 37 postnatal days (P) old Mongolian gerbils (*Meriones unguiculatus*) with a VT1200S Vibratome (Leica, Wetzlar, Germany) (table 2.1). The slices were transferred to an incubation solution (same as the slice solution for young animals but with 2 mM CaCl₂ and 1 mM MgCl₂) and kept at 36° C for 45 minutes, bubbled with 5% CO₂ and 95% O₂.

2.2 Electroporation

The electroporation procedure was similar to that described by Lang et al. (2006) and Nevian and Helmchen (2007). During electroporation, the slices were perfused

Table 2.1: Numbers and Ages of Animals and Neurons Used

Postnatal (P) day	P9-P10	P13	P17-P18	P21	P27	P36-P37	Total
Number of animals	2	2	3	2	2	2	13
Number of neurons	5	7	8	14	8	10	52

continuously with incubation solution at room temperature. Cells were electroporated under visual control of a CCD camera (TILL Photonics, Gräfelfing, Germany) mounted onto an upright micro scope (BX50WI, Olympus, Hamburg, Germany) equipped with gradient contrast illumination (Luigs and Neumann, Ratingen, Germany). Visually identified cells were approached with a glass pipette (tip diameter $\sim 1 \mu\text{m}$) filled with either Alexa Fluor 488 sodium hydrazide or its 568 analog (1 mM, Molecular Probes, Eugene, OR). Alexa hydrazide derivatives with low molecular weight were used so that small cellular processes such as spines and filopodia were readily labeled, allowing accurate detection (Lang et al., 2006; Nevian and Helmchen, 2007). The fluorescent dye-loaded pipette was pressed onto a selected cell and a single 18–20 ms long voltage pulse (15–20 V) was applied. The voltage pulse was generated by an EPC10/2 amplifier (HEKA Elektronik, Lambrecht, Germany) and post-amplified 10 times by a linear stimulus isolator (A395; World Precision Instruments, Berlin, Germany). Cell loading was visualized with a monochromator system (TILL Photonics). After 10–30 seconds the dye appeared evenly distributed within the dendrites of a given cell. Slices containing loaded cells were fixed in 4% paraformaldehyde overnight. After a 2×5 -minute wash with phosphate-buffered saline (PBS; pH 7.4), the slices were mounted in Vectrashield medium (H-100, Vector, AXXORA, Lörach, Germany) on glass slides with a small spatial separation of plasticine sealed under a coverslip with nail polish.

2.3 Cell Reconstruction

Image stacks of fluorescently labeled cells were obtained with a confocal Leica SP1 System by using a $63 \times$ objective with 1.32 NA, leading to a voxel size of $(310 \text{ nm})^2 \times$

325 nm. Images were processed by using AMIRA 4.1.1 software (Mercury Computer Systems, TGS Unit, Düsseldorf, Germany). As a first step, I imported the different image stacks of single cells and merged them to one stack. The skeleton of the neuron was compartmentalized as follows: branch points and end points, and if necessary, some points in between were set manually. This initialization approximates the shape of the neuron. The neuronal arborization was compartmentalized in three dimensions by using a computer-assisted software tool provided by Dr. Evers¹ (Schmitt et al., 2004; Evers et al., 2005). This software allows interaction with implemented automatic routines to maintain control and quality during compartmentalization.

The resulting data were stored in swc-format², which describes the neural morphology as a list of rows each describing a neural segment as a *compartment*. In each row a compartment is approximated as a cylinder, which is described by a compartment number, a type variable, the position of the cylinder's end point (in x, y, z Cartesian coordinates), its radius, and the number of the adjacent parent compartments on the path to the soma. The length of a compartment is defined as the Euclidian distance of the position of the cylinder's end point as given in the swc-format to the equivalent position of its parent compartment. This length was fixed during the tracing procedure to 0.5 μm . This simplifies the analysis, as a specific number of compartments can be matched to a specific distance. With this set of compartments (C), e.g., the *surface area* (2.1) *volume* (2.2), and *total cell length* (2.3) of each neuron can be calculated according to the following:

¹Freie Universität Berlin, <http://www.neurobiologie.fu-berlin.de/pflueger/evers.html>

²For specification see also: <http://www.neuronland.org/NLMorphologyConverter/MorphologyFormats/SWC/Spec.html>

$$\text{surface area} = \sum_{c \in C} 2\pi c_{\text{radius}} \cdot c_{\text{length}} \quad (2.1)$$

$$\text{volume} = \sum_{c \in C} \pi c_{\text{radius}}^2 \cdot c_{\text{length}} \quad (2.2)$$

$$\text{total length} = \sum_{c \in C} c_{\text{length}} \quad (2.3)$$

It also provides the tree structure of the neuron. The first compartment from a given tree was always placed in the center of the soma. This compartment is referred to as the *root compartment*. I derive from the tree structure the terminal degree of each compartment, which is part of my characterization of the dendritic arborization pattern (see Fig. 3.2). I defined the *terminal degree* of a given compartment as the sum of all *terminal tips* that finally emerge from it (Cuntz et al., 2007). The *terminal tip* is the end point compartment of a terminal branch. For example, if a compartment led to three final branches, it was assigned a *terminal degree* of three. The *terminal tip* itself was assigned a terminal degree of one.

This metric description of each neuron provided the basis for further data analysis, which was performed with custom-written software in Matlab 7.4 (TheMathWorks, Ismaning, Germany). All results are given as mean \pm standard error.

2.4 Tissue Alterations Imposed by the Experimental Procedure

Neuronal tissue tends to shrink when fixed with paraformaldehyde, and mounting of brain slices leads to flattening. Thus, the absolute values presented might be distorted by the experimental procedure. To determine the factor by which the tissue shrinks and flattens dependent on the developmental stage, I electroporated single cells under visual control and imaged these with a TILL Photonics system in acute brain slices.

From these images, I estimated the size of the cell bodies, the radius of dendrites, or distances between landmarks on dendritic trees (e.g., branch points).

I fixed the brain slices overnight in 4% paraformaldehyde. After a 2×5 -minute wash with PBS, the slices were placed on a slide, and the loaded cells were visualized under an upright fluorescence microscope (Axio ImagerM1, Zeiss, Oberkochen, Germany) with a $20 \times$ objective (0.5 NA). From these images, I determined again the cell size and the distances between the same landmarks as before. This procedure allows one to measure the extent of the shrinkage of the cell within the tissue, independent of the mounting artefacts. The shrinkage derived from the average of all measured distances gave a factor of 0.99 ± 0.03 and 0.92 ± 0.03 for P9 and P36, respectively (P9, 2 animals, $n = 4$ slices, 10 somata, 11 landmarks; P36, 2 animals, $n = 2$ slices, 4 somata, 5 landmarks).

I also assessed whether the mounting procedure described above affects the quantification of structures. The fully mounted brain slices were imaged with a confocal microscope (as above) by using a $25 \times$ objective with 0.75 NA (voxel size: $(390\text{nm})^2 \times 407\text{nm}$). From such image stacks, I obtained the same distance measurements as described before. Despite the plasticine separator, the flattening by the coverslip imposed a different effect on the two age groups. Slices of P36 animals continued to shrink more than they were affected by flattening. Together, shrinkage and flattening led to an overall difference that is described by a factor of 0.87 ± 0.02 . The brain slices of P9 animals were more affected by the flattening than by the mounting procedure, and the overall difference can be described by a factor of 1.12 ± 0.03 . The effects of shrinkage and flattening on the quantification presented are discussed below.

2.5 Multi-Compartmental Modeling

Simulations of multi-compartmental models were conducted using NEURON 7.0 (Hines, 1984, 1993; Hines and Carnevale, 2000, 2001; Hines et al., 2009) running with python 2.6 and Ubuntu Linux. Morphological data were exported in NEURON format (axons were not taken into account) dividing the morphology into three

partitions, namely the soma, the lateral dendrite, and the medial dendrite. Passive conductance was taken homogeneous distributed across the entire surface area. From now on, I will refer to the passive conductance as g_{rest} because it represents the total conductance of all active and passive channels during the state of resting potential. For specific membrane capacity, I used $c_m = 1 \mu\text{F}/\text{cm}^2$ for all simulations.

Synaptic inputs were simulated by homogeneously placing alpha-synapses with time constant $\tau_{\text{syn}} = 0.1 \text{ ms}$ along each dendritic tree. To avoid artefacts caused by specific locations synapses were placed at a regular distance of $0.5 \mu\text{m}$. The conductance amplitude of a synapse was chosen such that the maximal conductance at each dendritic tree was 100 nS.

3 Quantification of the Three-Dimensional Morphology

To quantify the morphology of neurons in the medial superior olive (MSO) and their developmental alterations, 52 cells from 13 animals at postnatal day (P) 9/P10 ($n = 5$), P13 ($n = 7$), P17/P18 ($n = 8$), P21 ($n = 14$), P27 ($n = 8$), and P36/P37 ($n = 10$) were subjected to a morphological analysis (Table 2.1, see also Appendix 6.2 for a timeline). These neurons were labeled with fluorescent dyes by single-cell electroporation (Lang et al., 2006; Nevian and Helmchen, 2007). The dendrites of these neurons were sufficiently dye loaded to take detailed image stacks for the subsequent compartmentalization. I focused on cells with their somata located in the center of the MSO plane irrespective of the number of primary dendrites. In general, these cells were bipolar (see below). The axonal origin was identified, but axonal compartments were excluded from further quantification.

3.1 Somatic Architecture of MSO Neurons

Examples of six individually electroporated cells from a transverse brain slice of a P21 gerbil are depicted in Figure 3.1A. The result of my compartmentalization procedure is illustrated in Figure 3.1B. This procedure captures cellular features seen in the confocal images, such as the somatic extent, small dendritic protrusions, and the axonal origin (Fig. 3.1A–C_{1–3}).

I quantified the somatic length and diameter (Fig. 3.1D,E). The distributions contain pooled data from all age groups tested. A Gaussian fit revealed a mean somatic

3 Quantification of the Three-Dimensional Morphology

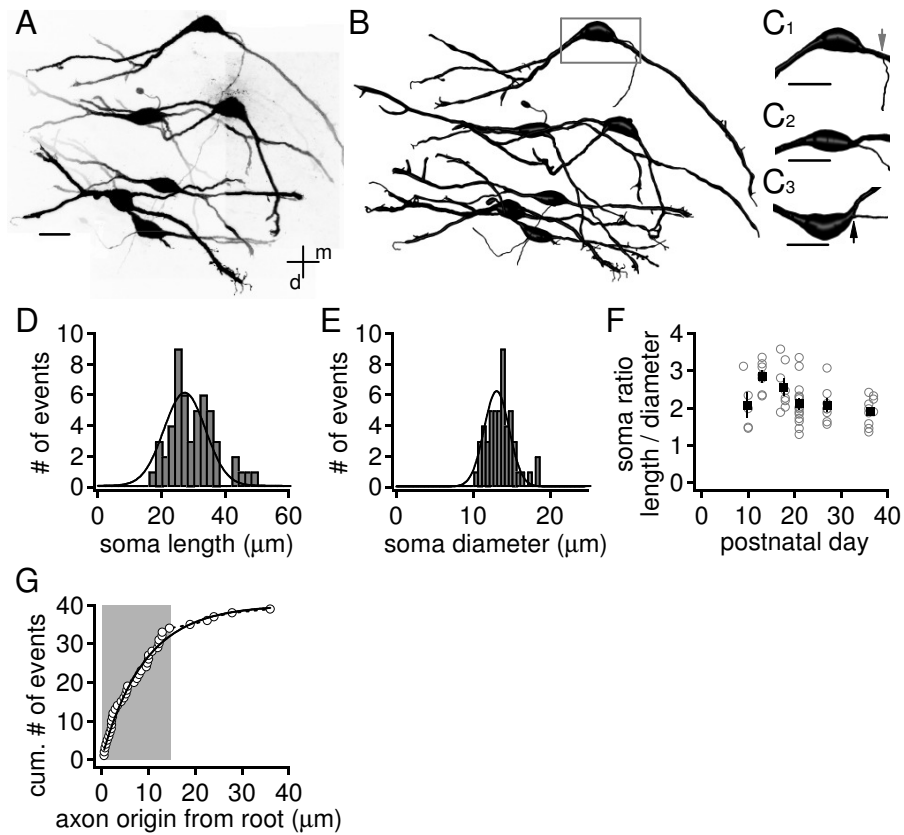


Figure 3.1: Somatic morphology of individually labeled neurons of the medial superior olive (Rautenberg et al. (2009), Fig. 1). **A:** Maximum projection of confocal images displaying six electroporated medial superior olive neurons at age P21, oriented along the dorsoventral nucleus axis (m, medial; d, dorsal). **B:** Compartmentalization of neurons shown in A. Note: due to perspective distortion (as this is a perspective three-dimensional illustration and not a maximum projection), no scale bar is added. **C₁₋₃:** Soma with axon (labeled in B) viewed from three different perspectives (each rotated by 60° around an imaginary axis along the soma and parallel to the scale bar, located in all three cases at same depth as the soma). Determination of axonal origin can be obstructed by overlying structures like dendrites (C₁, gray arrow) and is correctly judged by this three-dimensional analysis (C₃, black arrow). **D:** Distribution of cell soma length (bin width: 2 μm, $n = 52$) fitted by a Gaussian (solid line). **E:** Distribution of maximal soma diameter (bin width: 0.5 μm, $n = 52$) fitted by a Gaussian (solid line). **F:** Somatic ratios of length and diameter as a function of postnatal age (open symbols represent individual cells; squares represent age group averages). **G:** A cumulative frequency plot of the location of axonal origin ($n = 39$). Shaded region corresponds to the average somatic area, and black line indicates exponential fit. **Scale bars:** 20 μm in A (applies to A and B) and C.

length of $27\ \mu\text{m}$ and a mean diameter of $13\ \mu\text{m}$ (Fig. 3.1D,E; $n = 52$). Independent of age, all somata appeared elongated, with an average ratio of length to diameter ranging from 1.9 to 3.0 (Fig. 3.1F).

3.2 Axonal Origin of MSO Neurons

The location of the axonal origin has been debated (Kiss and Majorossy, 1983; Smith, 1995; Kuwabara and Zook, 1999; Scott et al., 2005). Therefore, I used my three-dimensionally compartmentalized neurons to specify the exact location of the axonal origin (Fig. 3.1C₁₋₃). In total, I could recover axonal origins in 39 neurons. In 34 of these neurons (87%), visual inspection suggested that the axon originates from the soma. In the other five cases, the axon origin was located on a primary dendrite. In order to quantify the location in more detail, I show a frequency plot of the distance between axonal origin and soma center (*root compartment*). For the present population, the axon emerges within the shaded region in 85% of cells (Fig. 3.1G) which marks half of the mean soma length of the respective neurons ($15\ \mu\text{m}$). The cumulative distribution of axonal origins could be fitted with an exponential function with a length constant of $9.1\ \mu\text{m}$ (Fig. 3.1G). Our data suggest that MSO neurons are elongated and their axons originate almost exclusively from somatic sites.

3.3 Developmental Changes in the Dendritic Arborization Pattern

An extensive refinement in the dendritic arborization between P9 and P36 (Fig. 3.2A–C) was apparent in my sampled neurons. In the depicted P9 neuron (Fig. 3.2A), the dendritic tree contains 139 terminal branches. This is about four times more than the 35 terminal branches shown for the P18 neuron (Fig. 3.2B) and about six times more than the 19 terminal branches of the P27 neuron displayed (Fig. 3.2C).

To quantify the arborization pattern of the dendritic trees, I counted the occurrence of compartments with respect to their distance to root as a function of their

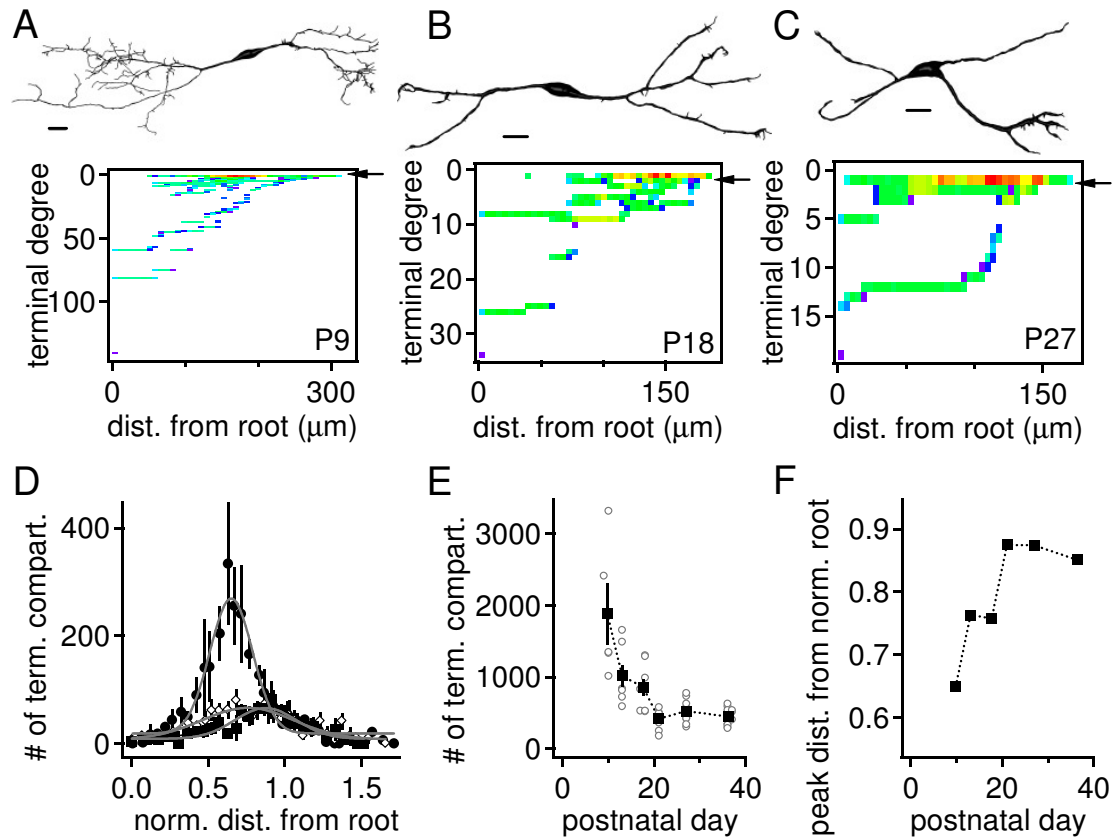


Figure 3.2: Pattern of dendritic arborization (Rautenberg et al. (2009), Fig. 2). **A–C:** Compartmentalized neurons of different postnatal ages (P9, P18, and P27 top panel; scale bar is at somatic depth) and their corresponding histograms of the number of compartments with a specific terminal degree over binned distance from soma center. Color code indicates the number of compartments in a given terminal degree – distance – bin ranging from low values (blue) to high values (red). Arrows point at terminal degree one. **D:** Histogram of terminal compartments plotted against the normalized distance from root, which was derived from each neuron’s average main dendritic length. Solid circles, P10; open diamonds, P18; solid squares, P27; gray curve indicates a Gaussian fit (bin width corresponds to $10 \mu\text{m}$). **E:** Number of terminal compartments of individual neurons (open circles) and the average of an age group (solid squares) as a function of postnatal days. **F:** Mean of the Gaussian fit (from D) indicates a relative shift of the main region of terminal compartments over age. **Scale bars:** $20 \mu\text{m}$ in A–C.

terminal degree (Fig. 3.2A–C; see Materials and Methods for a definition of *root compartment* and *terminal degree*). By analyzing the distribution of compartments with a terminal degree of one (Fig. 3.2A–C, black arrows), I found a reduction of the number of terminal compartments from $1,887 \pm 429$ (P10, $n = 5$) to 448 ± 40 (P36, $n = 10$) over the developmental period (Fig. 3.2D,E). In non matured cells, the largest number of terminal compartments appeared in the medial dendritic area. To quantify this finding, I normalized the compartment distance to the average length of the main dendrites of a given cell. These normalized distributions were fitted by a Gaussian to extract the mean of the relative distances of the accumulation of terminal compartments (Fig. 3.2D, gray lines, for three representative age groups). The maximum of this distribution indicates an average distance of dendritic branches that corresponds to 70% and 90% of the average length of the main dendrites in P10 and P21 gerbils, respectively (Fig. 3.2F). Therefore, the remaining arborization makes relative shifts toward more distal parts of the dendrite during development.

These results demonstrate a dendritic refinement over the developmental period during which the number of terminal compartments becomes reduced and the remaining branches localize at distal parts of the main dendrites.

3.4 Quantification of the Overall MSO Cell Architecture

The reduction of the number of terminal compartments should also be reflected by an overall reduction in total cell length and the number of branch points. Indeed, the number of branch points decreased during development from 160 ± 29 (P10, $n = 5$) to 24 ± 4 (P36, $n = 10$) with a time constant of about 3.3 days (Fig. 3.3A). The total cell length changed from $1,959 \pm 345 \mu\text{m}$ to $581 \pm 44 \mu\text{m}$ (Fig. 3.3B) over the same developmental period. This decline was slower ($\tau = 5.4$ days) than the loss of dendritic branch points, which implies that the initial reduction of branch points is mainly due to the loss of branches of short length. This was verified by calculating the mean length of all terminal branches over the developmental period

(Fig. 3.3C). The mean length of a terminal branch increases about twofold within the developmental period investigated.

The area of the cell surface is a crucial parameter for computational models (Rall et al., 1992; Mainen and Sejnowski, 1996; Agmon-Snir et al., 1998; Grau-Serrat et al., 2003; Zhou et al., 2005; Dasika et al., 2007; Cuntz et al., 2007). I found that the total surface area of the cell decreased during development (Fig. 3.3D). Assuming a specific membrane capacity of $1 \mu\text{F}/\text{cm}^2$ (Curtis and Cole, 1938), I calculated that the cell capacitance decreased from $\sim 75 \text{ pF}$ (P10) to $\sim 55 \text{ pF}$ (P36).

Because the cell length and surface area decrease during the developmental period, a reduction in cell volume might be expected. However, I find that the average volume of the MSO neurons increases by a factor of 1.5 from its initial value of $4.409 \pm 217 \mu\text{m}^3$ (P10, $n = 5$, Fig. 3.3E) during postnatal development. This finding indicates a developmental change in the volume-to-surface-area ratio (for cylinder-like structures: $\text{volume}/\text{surface area} \sim \text{radius}$). A change in somatic volume can be excluded, because I found the overall soma shape to be constant during late postnatal development (Fig. 3.1F).

Therefore, I analyzed the developmental change in the average dendritic radius as a potential source of a change in volume-to-surface-area ratio. Figure 3.4A shows that the dendritic radius, as a function of the normalized distance from the soma center to each individual terminal tip (Cuntz et al., 2007), increased with age. I also analyzed the proximal and distal areas of the dendrites separately (Fig. 3.4A, gray areas and inset, and Fig. 3.4B). The dendritic radius increases by a factor of 2 at distal (ii) compared with proximal (i) regions (Fig. 3.4B, slope of solid gray line). The average radii of the proximal and distal sites in mature animals are $1.71 \pm 0.02 \mu\text{m}$ and $1.39 \pm 0.01 \mu\text{m}$, respectively (P36, $n = 10$). This finding shows that the final dendritic radius is established late in development at P27. The increase in dendritic radius helps to explain the substantial change in volume-to-surface-area ratio as described above. This analysis indicates that MSO neurons reach the adult stage around P27, and that the neurons become morphologically compact and cylinder-like.

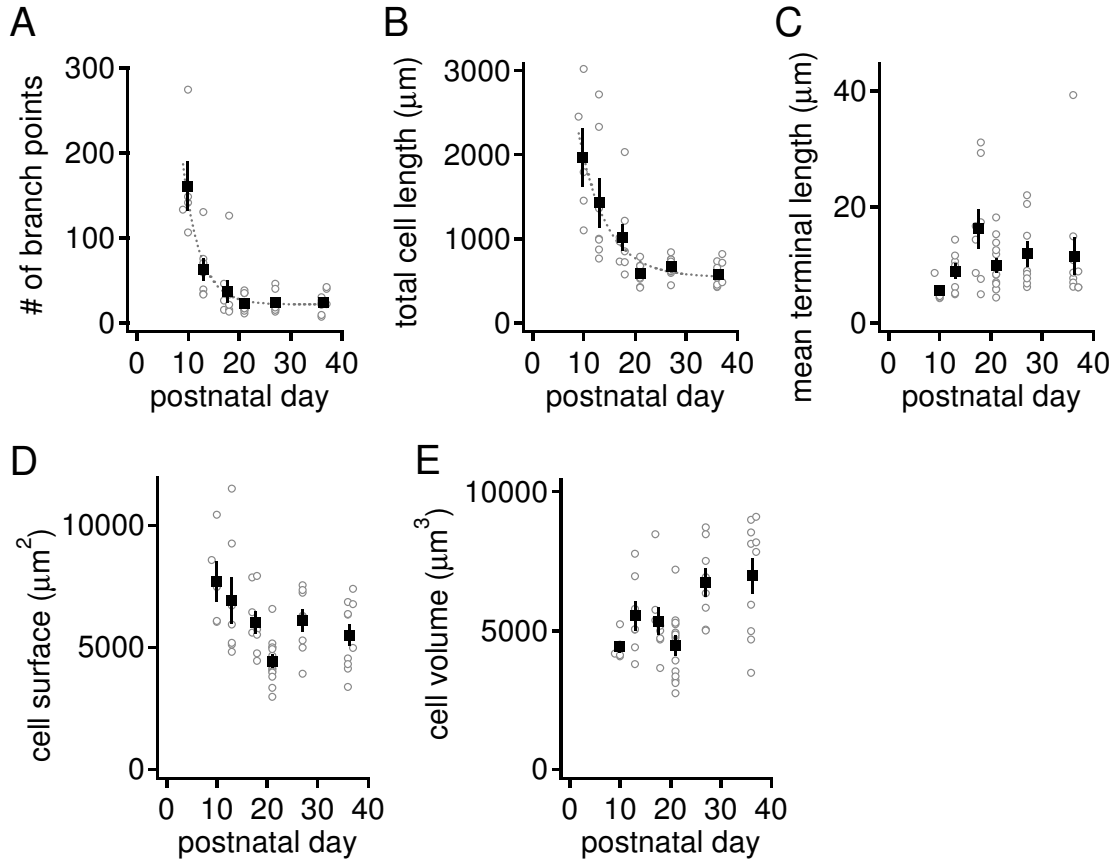


Figure 3.3: Morphological parameters change during development (Rautenberg et al. (2009), Fig. 3). **A:** Developmental change in numbers of branch points. Gray dotted line indicates exponential fit. **B:** Total cell length given as the sum of the length of all compartments is plotted as function of development. Gray dotted line represents exponential fit. **C–E:** Developmental profile of the mean length of terminals (C), cell surface area (D), and volume (E). Open symbols represent individual cells, and squares represent average values of a given age group (P9/P10, $n = 5$; P13, $n = 7$; P17/P18, $n = 8$; P21, $n = 14$; P27, $n = 8$; P36/P37, $n = 10$)

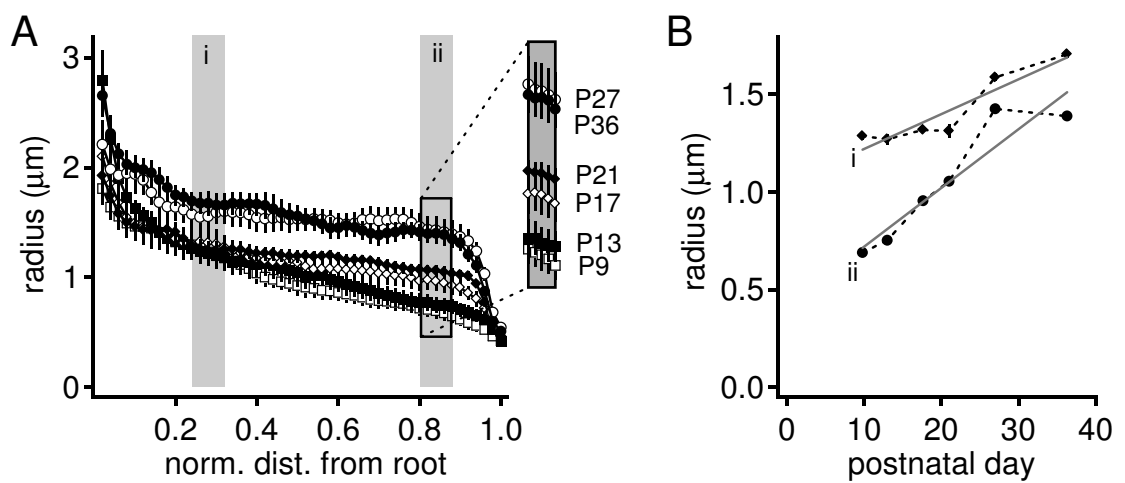


Figure 3.4: *Maturation of dendritic thickness (Rautenberg et al. (2009), Fig. 4).* **A:** Mean of dendritic diameter of neurons of a given age group as a function of the normalized path from soma center (root) to terminal tip compartment. The inset shows a magnification of the changes of the dendritic radius at a distal region indicated by the box. **B:** Radius of proximal (i) and distal (ii) dendritic regions as a function of postnatal development extracted from the shaded areas in A(i) and A(ii), respectively. Gray lines represent linear fits.

3.5 Metric Criterion of Filopodia

Besides full branches, dendrites possess appendages such as filopodia-like structures. A developmental loss of a certain type of appendages might be responsible for the changes in the dendritic tree structure described (Figs. 3.2, 3.3). Thus, it would be possible that the reduction in total cell length is due to a loss of specific dendritic processes such as filopodia. In the following, I search for a metric criterion that allows to separate different dendritic appendages, such as filopodia-like structures, from full branches. Assuming that different types of protrusions possess a specific diameter and length, these candidates should be separable from normal dendritic branches.

Therefore, I analyzed the radius of the dendritic compartments as a function of the distance to its terminal tip. Figure 3.5A₁ gives an example of two dendritic branches (black (i) and dark gray (ii)) that are separately depicted below (Fig. 3.5A₂). For these examples the dendritic radius of a compartment is given as a function of its distance to the terminal tip (Fig. 3.5B). This function was convolved with a Gaussian kernel ($\sigma = 0.5 \mu\text{m}$, not shown) and differentiated with respect to distance (Fig. 3.5C, same color code). In order to determine characteristic length of possible filopodia, the mean of all slopes for all terminal tips was calculated (Fig. 3.5D). The minimum closest to the tip provides the length of interest (Fig. 3.5C shaded area). For the depicted P10 cell I derived a characteristic length of $7.5 \mu\text{m}$ from the terminal tip which would separate different appendages. Next, I analyzed for all terminal tips of this cell the maximal slope within this characteristic length. If a distribution of these maximal slope values would result in two distinct populations then filopodia-like structures could be separated from normal dendritic branches. However, we could not separate distinct populations from the resulting histogram (Fig. 3.5E). This analysis was carried out for all cells with more than 100 branches ($n = 7$) because only in those can a reasonable distribution be extracted. All cells shared a similar characteristic length of protrusion ($7 \pm 0.5 \mu\text{m}$; $n = 7$) and the maximal slope was distributed in a single population. Thus, I suggest that within the compartmentalized dendrite all structures share a similar morphological weight. Therefore, an equal

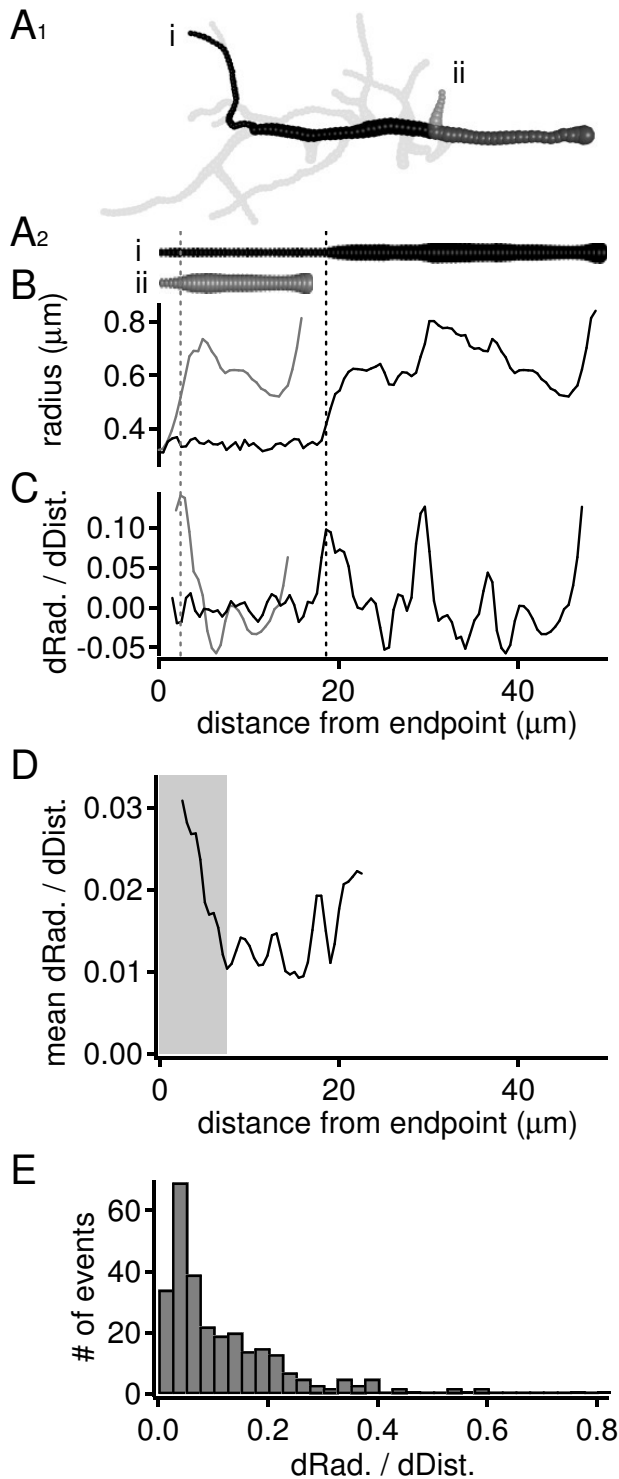


Figure 3.5: *Dendritic appendages* (Rautenberg et al. (2009), Supp. Fig. 2). **A₁**, **A₂**: An example of two dendritic branches (black (i) and dark gray (ii)) that are separately depicted below. **B**: For the two examples of (**A₁**), the dendritic radius of a compartment is given as a function of its distance to the terminal tip. **C**: This function was convolved with a Gaussian kernel ($\sigma = 0.5 \mu\text{m}$, not shown) and differentiated with respect to distance (same color code). **D**: In order to determine characteristic length of possible filopodia, the mean of all slopes for all terminal tips was calculated. The minimum closest to the tip provides the length of interest (C shaded area). For the depicted P10 cell I derived a characteristic length of $7.5 \mu\text{m}$ from the terminal tip which would separate different appendages. Next, I analyzed for all terminal tips of this cell the maximal slope within this characteristic length. If a distribution of these maximal slope values would result in two distinct populations then filopodia-like structures could be separated from normal dendritic branches. **E**: However, I could not separate distinct populations from the resulting histogram. This analysis was carried out for all cells with more than 100 branches $n = 7$ because only in those can a reasonable distribution be extracted. All cells shared a similar characteristic length of protrusion ($7 \pm 0.5 \mu\text{m}$; $n = 7$) and the maximal slope was distributed in a single population.

treatment of all compartments, leading to an estimate of the developmental profile of cell features, such as branch point number or total cell length (Fig. 3.3), becomes valid.

3.6 Distribution of Surface Area and its Development

The distribution of surface area (area of the plasma membrane) along the cell's main axis is an important property for defining the cell's organization, orientation, and potential synaptic input area. I analyzed the amount of surface area of MSO neurons along their principal axis, irrespective of their arborization pattern.

I first used principal component analysis (PCA) to calculate the principal axis of the cell, and I transformed the coordinates of each individual compartment into a new coordinate system with respect to this axis. This procedure enables us to align cells of the same age group by orienting the dendritic tree along the main axis. An example of this transformation is given in Figure 3.6A–C. A compartmentalized cell (Fig. 3.6A,B) was aligned along its principal axis and is shown as a two-dimensional projection (Fig. 3.6C). After alignment, I binned the surface area of the cell along its principal axis. In addition, I divided the neuron into two sides at the point of origin. Then I normalized each side to the maximal value of the principal components (Fig. 3.6D). This allowed us to estimate the distribution of surface area of the cell along its principal axis. The shaded region in Figure 3.6C illustrates the summation of the surface area derived from all compartments at a given distance. In accordance with my previous results (Fig. 3.3), I find that the total membrane area decreases with age (Fig. 3.6E). Also, a relative shift from a more centrally located membrane accumulation to a more distal membrane accumulation along the principal axis is apparent (see also P10 example neuron depicted in Figure 3.6A–D).

The measurements obtained demonstrate that the dendritic orientation of MSO neurons is bipolar, irrespective of the number of primary dendrites. I inferred this from the fact that the spatial extension measured with the absolute values of the PCA (e.g., $239 \pm 9 \mu\text{m}$ for P36) is nearly equal to twice the length of the average

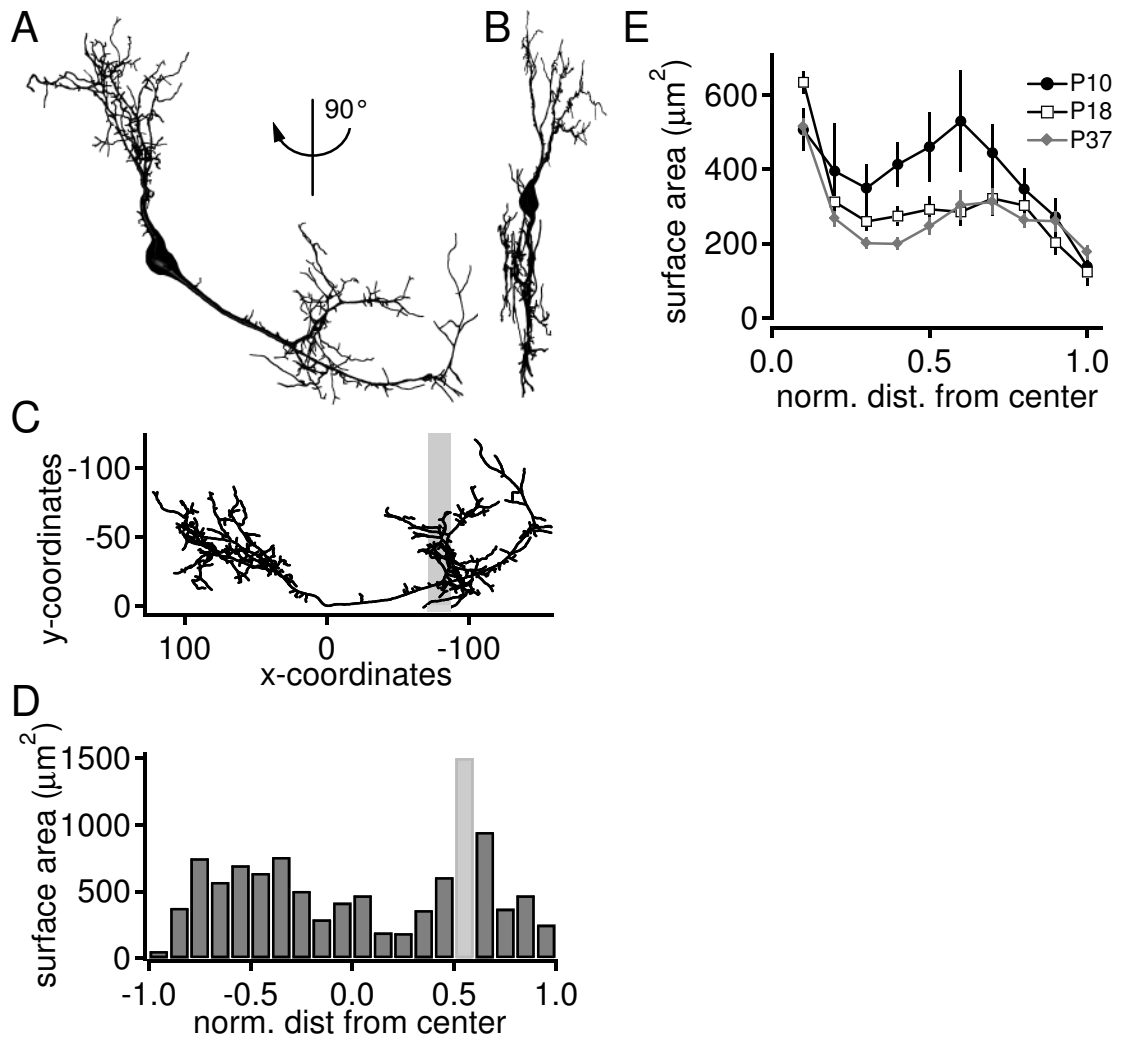


Figure 3.6: Surface area distribution of medial superior olive neurons (Rautenberg et al. (2009), Fig. 5). **A,B:** Three-dimensional illustration of a multi-compartmental model (A) rotated by 90 (B) to visualize the three-dimensional extent. Note: due to perspective distortion (as this is a perspective three-dimensional illustration and not a maximum projection) no scale bar is added. See x-y-coordinates in C to estimate the extent of the cell. **C:** Same neuron as in A and B plotted as skeleton aligned along its principal axis (x-coordinates in μm). Gray area indicates region in the single bin highlighted in D. **D:** Histogram of cell surface area along the principal axis (bin size 0.1 of the normalized distance of the principal axis extent). **E:** Profile of the surface area for P10, P18, and P37 as a function of normalized distance from soma center along the principal axis.

3.6 Distribution of Surface Area and its Development

main dendrites (absolute value from the analysis presented in Figure 3.2, e.g., $2\times$ ($130 \pm 13 \mu\text{m}$) for P36). Thus, in the gerbil MSO, the main dendrites extend in a bipolar fashion from the soma with a minor three-dimensional extent.

4 Electrophysiological Properties, Symmetry, and Coincidence-Detection-Characteristics of MSO Morphologies

The second part of my thesis focused on electrophysiological properties, symmetry aspects, and coincidence-detection-characteristics during late postnatal development. Those morphologies were that I already analyzed in the preceding chapter. The reconstructions of these morphologies were the basis for multi-compartmental computer simulations of electrophysiological experiments: first, it was quantified how morphologies of varying ages modulate the effect of resting conductance (g_{rest}) and axial resistivity (ρ) on the passive electrophysiological properties input resistance (R_{in}) and effective decay time constant (τ_{eff}). I estimated passive parameters according to published electrophysiological data of MSO neurons Magnusson et al. (2005); Scott et al. (2005). Using these estimated parameters, I correlated electrophysiological properties with metric properties. Second, I compared lateral with medial dendritic trees with respect to metric and electrophysiological properties. And third, I investigated the coincidence-property of morphologies by simulating equally distributed synapses across each dendrite. See Appendix 6.1 for a timeline.



Figure 4.1: Illustration of a simulation of a current clamp experiment to calculate input resistance (R_{in}) and effective membrane time constant (τ_{eff}) of a multi-compartmental model.

4.1 Influence of Passive Conductance and Axial Resistivity on Input Resistance and Effective Membrane Time Constant

Using a passive multi-compartmental model of each neuron with specific membrane capacity (c_m), resting conductance (g_{rest} , representing the total conductance of all active and passive channels during the state of resting potential), and axial resistivity ϱ , I simulated somatic current clamp experiments¹ (Fig. 4.1A). Rectangular current pulses of $I = -1$ nA were injected at the soma and voltage responses of the models were recorded at the injection site (Fig. 4.1, inset). Fitting an exponential to the first 2 ms of this voltage trace after stimulus onset, I derived the input resistance ($R_{in} = \Delta V/I$) and the decay time constant (τ_{eff}) of each model, where ΔV denotes the *amplitude* of the voltage response.

Figure 4.2A and B show the mean of R_{in} and τ_{eff} , respectively, for all models grouped across ages and four different combinations of g_{rest} and ϱ . An increase in ϱ seems to increase the input resistance R_{in} and to decrease decay time τ_{eff} . A decrease

¹For more detail about c_m , g_{rest} , and ϱ see formular 1.1 and chapter 2.5

in g_{rest} leads to an increase in input resistance R_{in} and an increase in decay time constant τ_{eff} . Compared to this, the differences of the morphologies across ages have a small effect which I describe in more detail later.

For a more detailed analysis of the influence of ϱ , I determined the input resistance R_{in} (Fig. 4.2C) and decay time τ_{eff} (Fig. 4.2D) for three example morphologies, varying ϱ between $10 \Omega \cdot \text{cm}$ and $400 \Omega \cdot \text{cm}$ while keeping g_{rest} constant at $3 \text{ mS}/\text{cm}^2$. An increase in ϱ leads to a monotone increase in R_{in} whereas the effect on τ_{eff} is non-monotone and has a minimum. The minimum of τ_{eff} depends on the specific underlying morphology (Fig. 4.1E). For $\varrho = 0$ the decay time τ_{eff}^0 is that of a point neuron: $\tau_{\text{eff}}^0 = c_m \cdot r_{\text{rest}} = \frac{c_m}{g_{\text{rest}}} = \frac{1 \mu\text{F}/\text{cm}^2}{3 \text{ mS}/\text{cm}^2} = 0.33 \text{ ms}$, with specific membrane capacity c_m and specific membrane resistivity r_{rest} .

For very large ϱ , τ_{eff} reaches the asymptotic value $\tau_{\text{eff}}^{\text{inf}}$, as no current can flow into the dendrites and therefore the effective morphology is reduced to one compartment with $\tau_{\text{eff}} = \tau_{\text{eff}}^0$. With decreasing ϱ , dendrites start to act as current sinks as current can flow into the dendritic branch, and therefore τ_{eff} gets faster. The same behavior can be observed in a simpler model with reduced number of compartment: one compartment representing the soma and 2 equal compartments representing the dendrites (Fig. 4.2D, inset), which was already theoretically described (Rall, 1960). Each dendritic compartment is connected with a resistance R_a to the soma. To compare Figure 4.2D with its inset, I estimate the resistance of a dendrite with a diameter of $d = 2.5 \mu\text{m}$ and length of $l = 50 \mu\text{m}$ which is comparable with the first unbranched part of a MSO neuron. For $\varrho = 400 \Omega \cdot \text{cm}$ the dendrite has a length resistance across its entire extent of $\varrho \cdot \frac{l}{\pi \cdot (d/2)^2} = 40.74 \text{ M}\Omega$ which would correspond to R_a of the minimum time constant τ_{eff} in the inset of Figure 4.2E. The observed morphology thus aids fast temporal processing. The dip in τ_{eff} then corresponds to ϱ being in a range between $67.54 \Omega \cdot \text{cm}$ ($R_a = 6.87 \text{ M}\Omega$, left dotted line) and $1767.73 \Omega \cdot \text{cm}$ ($R_a = 180.06 \text{ M}\Omega$, right dotted line).

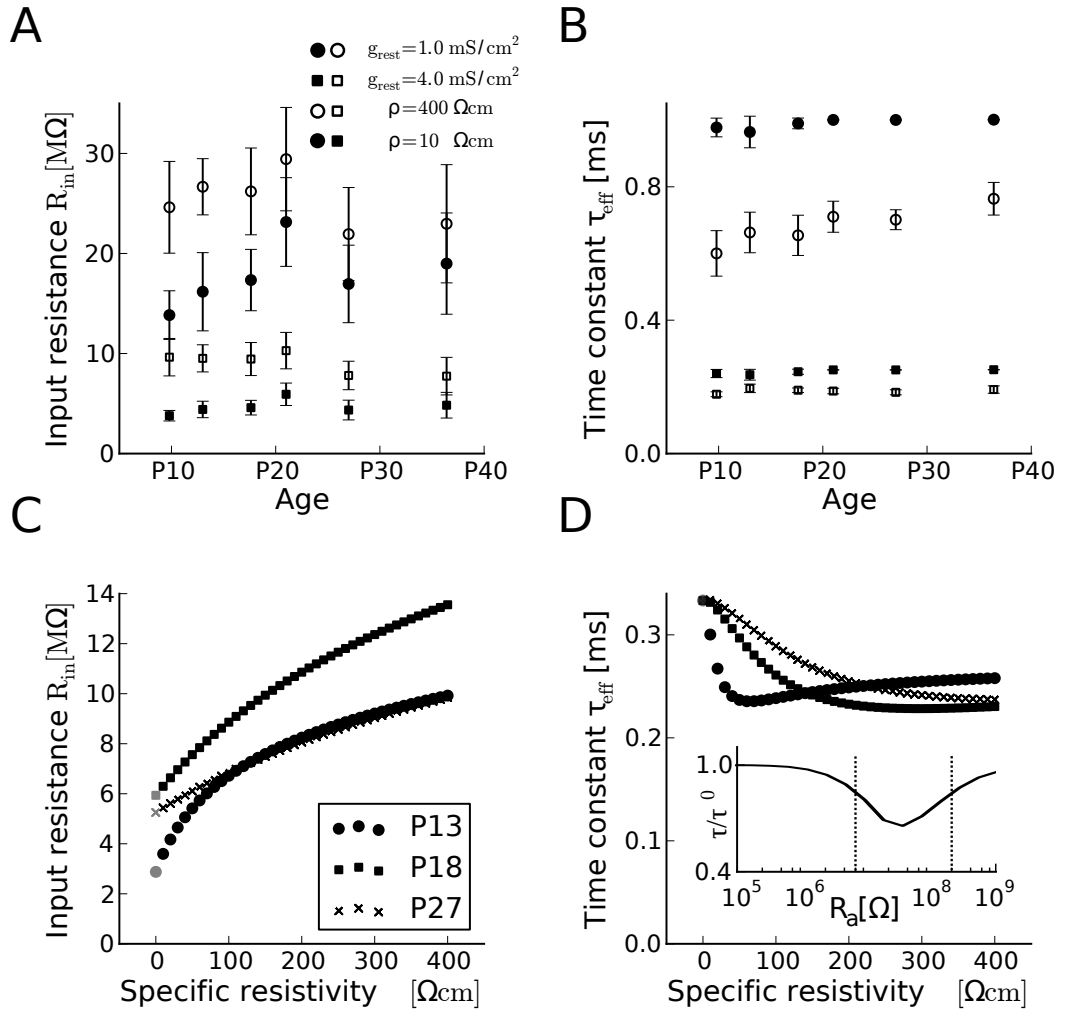


Figure 4.2: Input resistance (R_{in}) and effective time constant (τ_{eff}) for varying parameters. **A, B:** Population data R_{in} (A) and τ_{eff} (B) for 52 MSO-morphologies as a function of age for four different combinations of axial resistivity (ρ) and resting conductance (g_{rest}) (circle: $g_{rest} = 1.0 \text{ mS/cm}^2$, square: $g_{rest} = 4.0 \text{ mS/cm}^2$), filled: $\rho = 10 \text{ } \Omega \cdot \text{cm}$, open: $\rho = 400 \text{ } \Omega \cdot \text{cm}$): An decrease in ρ increases R_{in} (A) and decreases τ_{eff} (B). **C:** R_{in} as a function of ρ for three sample morphologies of different ages (circles: P13; squares: P18; crosses: P27; grey initial values: calculated by surface area according to a model of a point neuron): R_{in} increases monotonic with increasing ρ . **D:** τ_{eff} as a function of (ρ) for three sample morphologies of different ages (see C): an increase of (ρ) has a non-monotone effect on τ_{eff} with a minimum which depends on the specific underlying morphology. *Inset:* a simplified three compartmental model with one compartment representing the soma and two equal compartments representing the dendrites. This model confirms the results of D. Here, each dendritic compartment is connected with a resistance R_a to the soma. For more details see last paragraph in section 4.1.

4.2 Estimation of Axial Resistivity

As demonstrated above, R_{in} is an important variable affecting the impact of morphology to the intracellular flow of current. Previous studies used $200 \Omega \cdot \text{cm}$ as a default value for their models of neurons of the MSO (Agmon-Snir et al., 1998; Zhou et al., 2005; Dasika et al., 2007). This value of $200 \Omega \cdot \text{cm}$ was never confirmed for neurons of the MSO.

In order to estimate axial resistivity (ϱ) I applied a method which makes use of eight measured combinations of input resistance (R_{in}) and effective time constant (τ_{eff}) (Fig. 4.3) from published data (Couchman et al., 2010)². I fitted all morphology to all of those combinations. For the successful fits, I plotted a histogram with ten bins across the range of resulting values for ϱ (Fig. 4.3B) and resting conductance (g_{rest} , for definition see section 4.1) (Fig. 4.3C). Here, ϱ is equally distributed between $10 \Omega \cdot \text{cm}$ and $110 \Omega \cdot \text{cm}$. The histogram for g_{rest} shows accumulations around $2.0 \text{ mS}/\text{cm}^2$ and $3.5 \text{ mS}/\text{cm}^2$. These results do not allow to conclude a specific value for ϱ .

Assuming an equally distributed set of combinations of R_{in} and τ_{eff} with R_{in} between $1 \text{ M}\Omega$ and $10 \text{ M}\Omega$ in steps of $0.5 \text{ M}\Omega$ and a constant τ_{eff} of 0.3 ms (Fig. 4.3D), I did the same analysis again (Fig. 4.3E,F). Figure 4.3E shows a minimum at a ϱ of $\sim 180 \Omega \cdot \text{cm}$ and the highest count below $50 \Omega \cdot \text{cm}$. Figure 4.4 shows ϱ and g_{rest} as function of R_{in} . Here, as expected, ϱ increases with age and g_{rest} decreases with age. However, a specific value for ϱ could not be estimated.

Therefore, I developed another approach to estimate ϱ and g_{rest} by the following method. The two measurements R_{in} and τ_{eff} are functions of both ϱ and g_{rest} . Consequently, I related my simulated results to experimentally measured R_{in} and τ_{eff} (Scott et al., 2005), and estimate the passive parameters of my model. Figure 4.5A,B shows iso- R_{in} -lines and iso- τ_{eff} -lines simulated with a morphology of an exemplary P27 neuron. For small R_{in} ($< 10 \Omega \cdot \text{cm}$) and small τ_{eff} ($< 0.5 \text{ ms}$) iso- R_{in} (Fig. 4.5A) and iso- τ_{eff} (Fig. 4.5B) lines would intersect with a steep slope. Thus, within this range, small changes of R_{in} and τ_{eff} do not strongly affect the point of the intersection making

²The age of corresponding gerbils was between P60 and P90

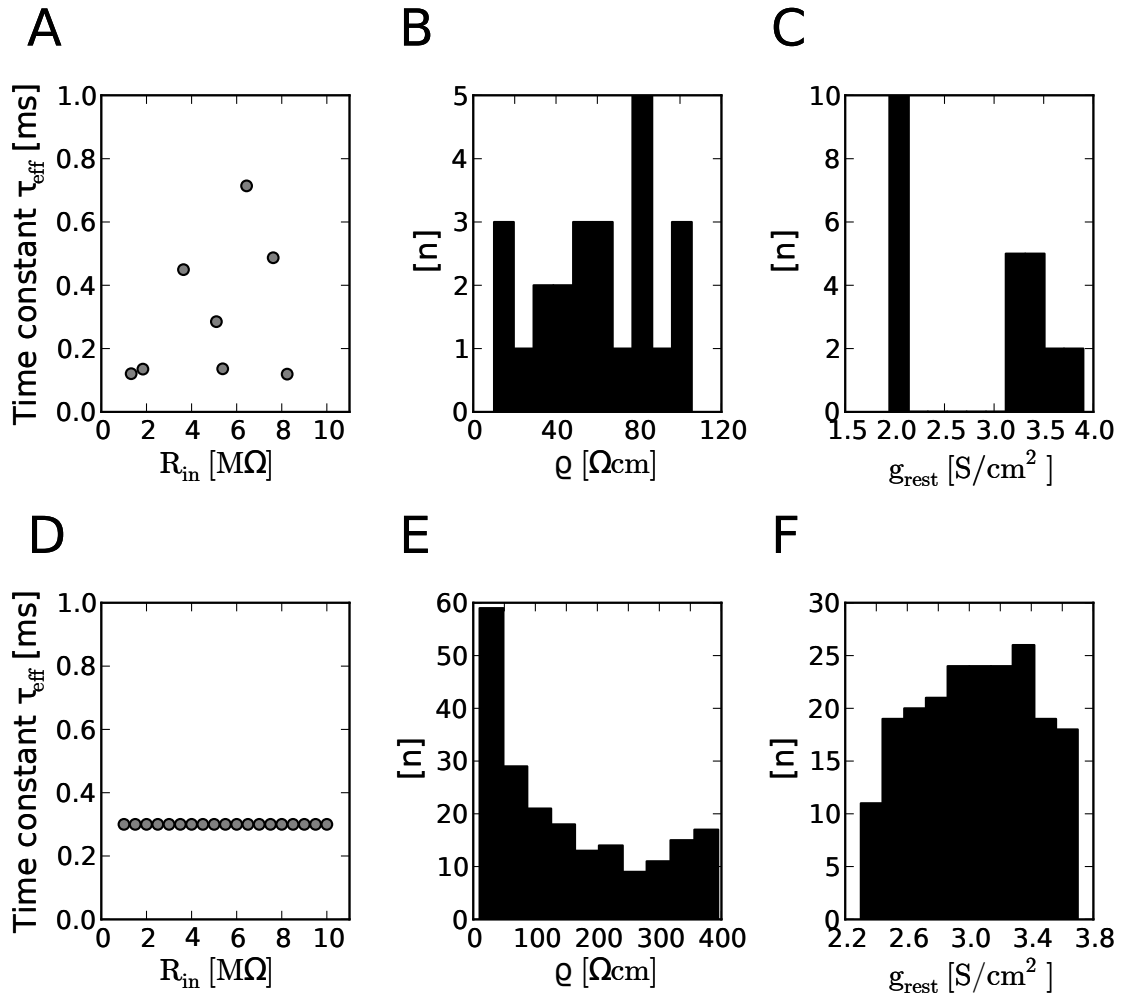


Figure 4.3: *Fitting axial resistivity and passive conductance to individual combinations of input resistance and time constant.* **A:** Combination of experimentally measured input resistance and time constant of eight measured cells from Couchman et al. (2010) (Input resistance: min=1.32 MΩ, max=8.24 MΩ, mean=4.95 ± 0.1162 MΩ; time constant: min=0.1196 ms, max=0.717 ms, mean=0.306 ± 0.010 ms). **B&C:** All models of adult cells where fitted to all combinations shown in A. The histograms counts all possible fits of specific axial resistivity B and passive conductance C, respectively. Where B shows equal distribution, C shows accumulations around 2.0 mS/cm² and 3.5 mS/cm². **D-F:** Here, the same analyses are applied for a different (and artificial) set of combinations of input resistances and time constants (combinations = {1, 1.5, ..., 10} × 0.3 [MΩ, ms]). E shows a minimum around 280 Ω·cm and the highest count below 50 Ω·cm. F shows a maximum around 3.4 mS/cm².

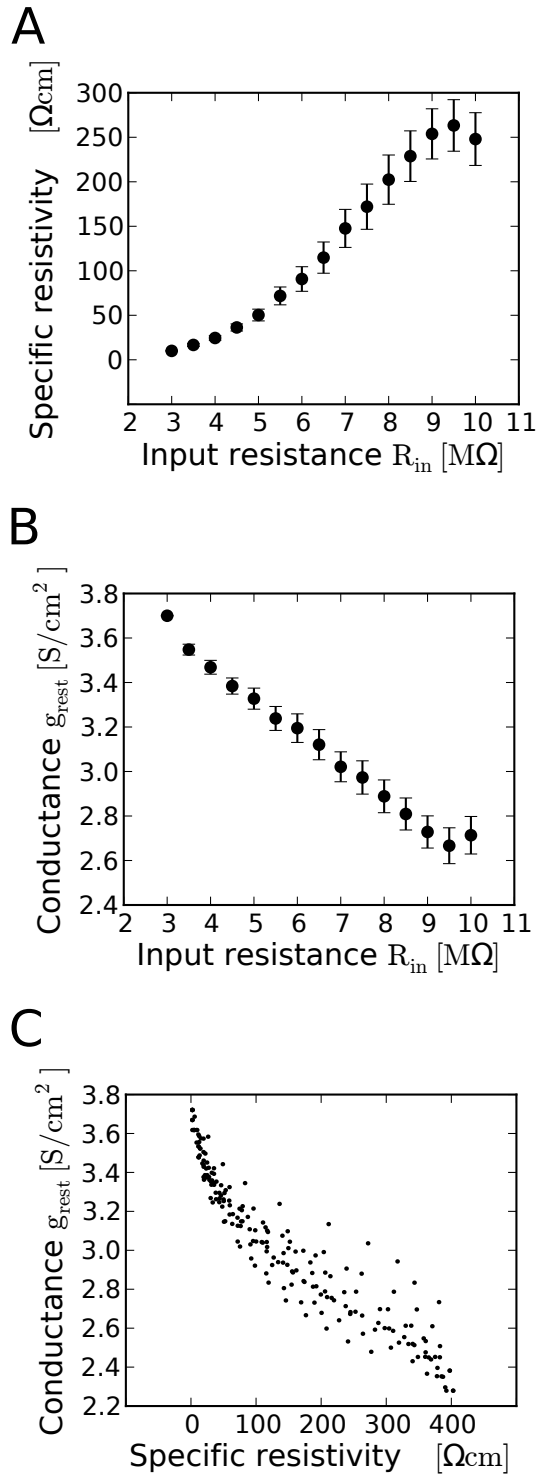


Figure 4.4: Distribution of specific resistivity ρ and passive conductance g_{rest} for underlying values from (Fig. 4.3D). **A:** Mean of ρ as a function of input resistance (R_{in}) (error bars: SEM). With increasing R_{in} , ρ increases from $\sim 10 \Omega\cdot\text{cm}$ to a maximum of $\sim 260 \Omega\cdot\text{cm}$. **B:** Mean of g_{rest} as a function of R_{in} (error bars: SEM). With increasing R_{in} g_{rest} decreases from $\sim 3.7 \text{ mS}/\text{cm}^2$ to **C:** Each point represents a combination of a morphology, ρ , and g_{rest} having one combination of Figure 4.3D as τ_{eff} and $R_{\text{in}} \sim 2.6 \text{ mS}/\text{cm}^2$

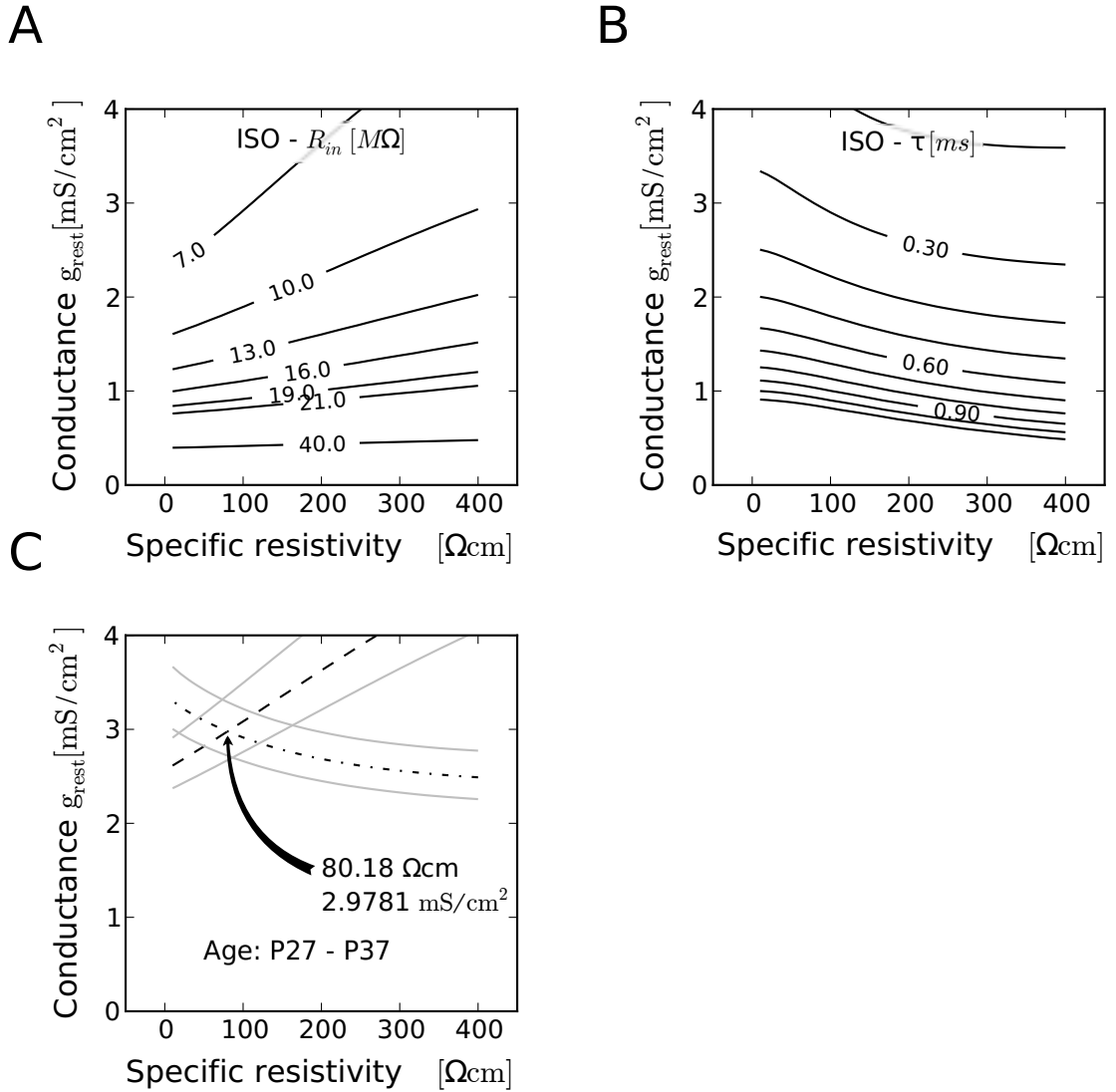


Figure 4.5: Estimation of ρ . **A:** Iso- R_{in} -lines of a sample morphology (P27): iso- R_{in} -lines for small R_{in} have a steeper slope than for higher R_{in} . **B:** Iso- τ_{eff} -lines of the same sample morphology (A): iso- τ_{eff} -lines for small τ_{eff} have a steeper slope than for higher τ_{eff} . **C:** Combinations of ρ and g_{rest} that lead to a constant mean R_{in} of 7.0 M Ω (dashed line), mean τ_{eff} of 0.3 ms (dotted line), and 10% error contours (gray lines) for all neurons \geq P27. The crossing shows the combination of $\rho = 80.18 \Omega \cdot \text{cm}$ and $g_{rest} = 2.9781 \text{ mS}/\text{cm}^2$ which leads to a mean R_{in} of 7.0 M Ω and a mean τ_{eff} of 0.3 ms which is an accordance with experimental findings from Scott et al., 2005.

the estimates of ϱ and g_{rest} less susceptible to noise within the data. From Scott et al. (2005) we know that R_{in} and τ_{eff} reach asymptotic values of $7 \text{ M}\Omega$ and 0.3 ms after about three weeks after birth³. Figure 4.5C shows combinations of ϱ and g_{rest} that lead to a constant mean R_{in} of $7.0 \text{ M}\Omega$ and mean τ_{eff} of 0.3 ms (black discontinuous lines). At the crossing of the iso-lines I find a combination of $\varrho \sim 80 \Omega \cdot \text{cm}$ and $g_{\text{rest}} \sim 3 \text{ mS}/\text{cm}^2$.

4.3 Estimation of Passive Conductance

In Figure 4.6A,B, R_{in} and τ_{eff} are almost independent of age despite the fact that during early postnatal development, neurons of the MSO change their morphology, e.g. surface area decreases and volume increases about 1.5 fold. In order to better investigate the influence of morphological changes on R_{in} and τ_{eff} during development, I compute modulation indices $M_R = \frac{R_{\text{in}} - R_{\text{in}}^0}{R_{\text{in}}^0}$ and $M_\tau = \frac{\tau_{\text{eff}} - \tau_{\text{eff}}^0}{\tau_{\text{eff}}^0}$ for further analysis. Here, R_{in}^0 and τ_{eff}^0 reflect the input resistance and effective time constant for punctified morphologies (with $\varrho = 0$). Therefore, the modulation index measures the influence of morphology on input resistance and time constant relative to a corresponding point neuron (with corresponding surface area). Keeping the estimated values for ϱ and g_{rest} constant at $80 \Omega \cdot \text{cm}$ and $3 \text{ mS}/\text{cm}^2$, M_R decreases with age from $\sim 65\%$ at P10 to an asymptotic value of $\sim 15\%$ at P21 (Fig. 4.6A, inset). M_τ increases from $\sim -20\%$ (P10) to an asymptotic value of $\sim -5\%$ at P21 (Fig. 4.6B, inset). This indicates that neurons “punctify” with age with respect to R_{in} and τ_{eff} .

The effect of maturation on the input resistance R_{in} is too small to explain the strong increase of input resistance with age observed physiologically at around two weeks after hearing onset (Fig. 4.6C). In order to estimate the mean R_{in} for ages between P9 and P21, I fitted an exponential function to data points from Magnusson et al. (2005) (Fig. 4.6C) assuming an asymptotic value of $7 \text{ M}\Omega$ Scott et al. (2005) for

³The cited study explores MSO neurons of P14 – P38 old gerbils (similar to the age of neurons used in the present study, P9 – P37). However, more recent findings from Couchman et al., 2010 report different values for gerbils between P60 and P90. For an analysis of those individual combinations of R_{in} and τ_{eff} , see Appendix.

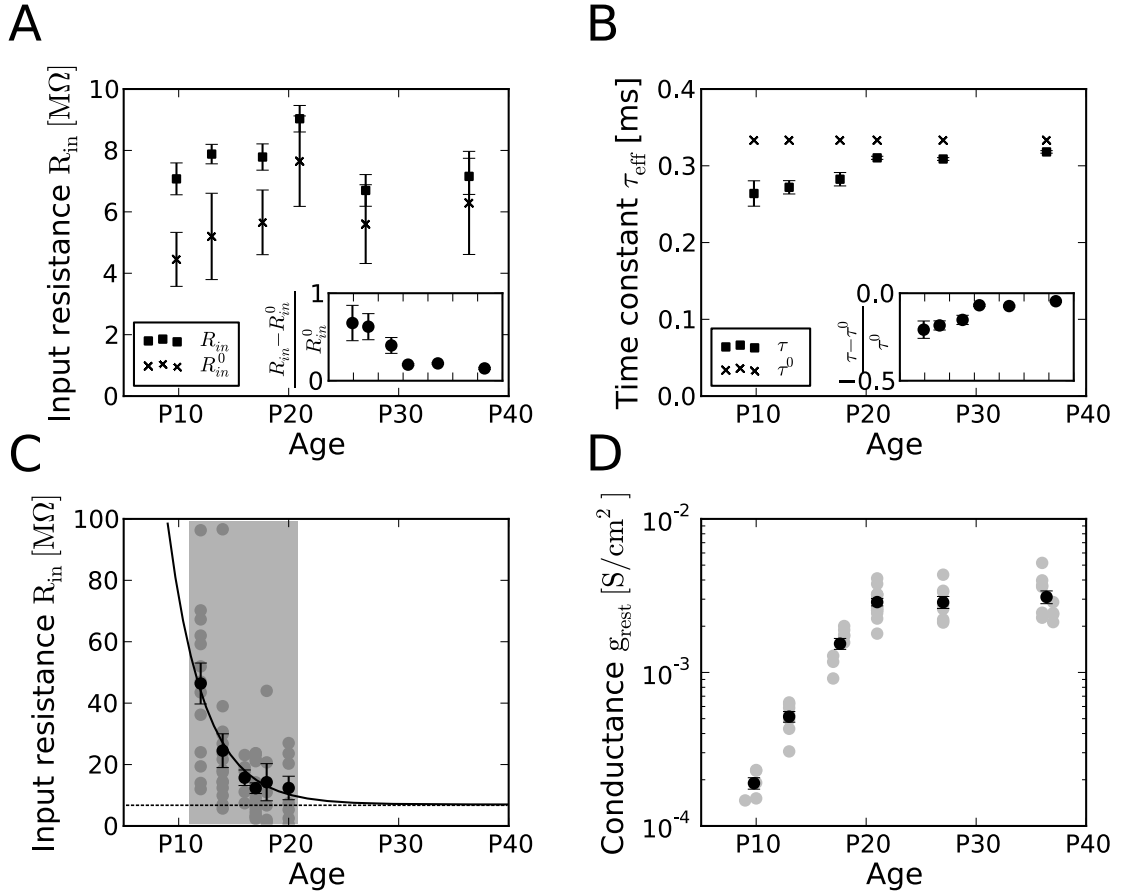


Figure 4.6: Modulation indices and estimation of g_{rest} . **A:** R_{in} as a function of age for all 52 morphologies for $\rho = 80 \Omega \cdot \text{cm}$ (squares) and $\rho = 0 \Omega \cdot \text{cm}$ (crosses). The difference between squares and crosses decreases with age. To illustrate this effect modulation index is computed ($M_R = (R_{in} - R_{in}^0) / R_{in}^0$, inset), which decreases with age. **B:** τ_{eff} as a function of age for all 52 morphologies with $\rho = 80 \Omega \cdot \text{cm}$ (squares) and $\rho = 0 \Omega \cdot \text{cm}$ (crosses). The difference between squares and crosses decreases with age. To illustrate this effect, the modulation index is computed ($M_\tau = (\tau_{eff} - \tau_{eff}^0) / \tau_{eff}^0$, inset): which converges towards 0 with increasing age. **C:** Population data of R_{in} (Magnusson et al., 2005) (gray points within the shaded region, P13 to P20). Black points show mean with SEM. Black line shows an exponential fit with a asymptote of 7 MΩ (dotted line) and $\tau_{eff} = 3.3$ days (Scott et al., 2005). **D:** Estimated g_{rest} as a function of age for each morphology (gray circles) that leads to an input resistance calculated by the fit (C) for the corresponding age. Black: mean g_{rest} with SEM for the corresponding age group.

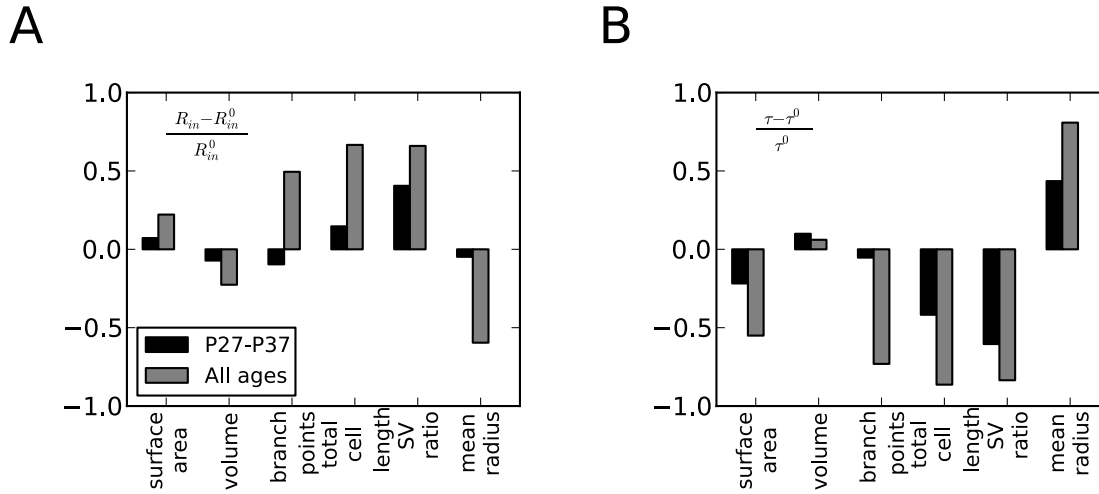


Figure 4.7: Correlation Between Metric and Electrophysiological Properties. **A:** Computed correlations of M_R with several properties of the morphological shape (surface area, volume, branch points, total cell length, surface-volume (SV) ratio, mean radius) for two different age groups (P27–P37: *mature ages*, black; P9–P37: *all ages*, gray). “All ages” show higher correlation than *mature ages* for all morphological properties. **B:** Computed correlations of M_τ with several properties of the morphological shape (see A for conditions). “All ages” show higher correlation than *mature ages* for all morphological properties except for volume.

mature neurons. Using the estimated $\rho = 80 \Omega \cdot \text{cm}$ for all models I estimated g_{rest} as a function of age. I found that g_{rest} increases 15 fold from $\sim 0.2 \text{ mS/cm}^2$ to $\sim 3 \text{ mS/cm}^2$, reaching asymptotic values at around P21. (Fig. 4.6D).

Note: In the following sections, I used $\rho = 80 \Omega \cdot \text{cm}$ and $g_{\text{rest}} = 3 \text{ mS/cm}^2$ across all ages. Doing so, I could focus on the effect of morphological properties and not the effect of changing passive parameters.

4.4 Correlating Electrophysiological with Metric Properties

To understand which morphological properties account for the observed changes in M_R and M_τ (Fig. 4.6A,B, insets), I computed how they correlate with proper-

Table 4.1: Results according to Fig. 4.8 (with L : lateral; M : medial; Δ : $L - M$)

Measure	P27 P37				all ages			
	mean _L	mean _M	Δ	p	mean _L	mean _M	Δ	p
Volume [μm^3]	2073.566	1564.016	509.540	0.024	1580.029	1332.889	247.139	0.011
Surface Area [μm^2]	2689.959	2093.981	595.978	0.010	2676.786	2246.124	430.662	0.002
Branch Points [#]	13.222	9.444	3.778	0.051	22.538	19.865	2.673	0.176
Total Cell Length [μm]	326.443	261.438	65.005	0.008	482.462	399.015	83.447	0.020
Surface-Volume-Ratio [$1/\mu\text{m}$]	1.357	1.409	-0.053	0.331	1.782	1.754	0.028	0.543
Mean Radius [μm]	1.258	1.222	0.035	0.437	0.994	0.986	0.008	0.677

ties of the morphological shape like surface area, volume, branch points, total cell length, and mean radius. I analyzed these correlations for two different ranges of age (Fig. 4.7), *mature ages* (P27–P37, with small alterations) and *all ages* (P9–P37, with a high variability caused by strong developmental alterations during early development): Across *mature ages* the correlations are smaller compared to *all ages* for all quantities, which reflects the reduced variability of morphologies. For *mature ages* the highest correlation with M_τ and M_R is found for the surface-volume-ratio. Across *all ages* most quantities correlate with input resistance (Fig. 4.7A) as well as with the effective time constant (Fig. 4.7B): volume and surface area correlate least whereas surface-volume-ratio, total cell length, and mean radius have strongest influence on M_τ and M_R . Hence, the latter – compared to *volume* and *surface area* – are more suitable measures of morphological shape which indicate that shape influences the electrophysiology of MSO neurons for the given ϱ , g_{rest} , and c_m .

4.5 Asymmetry of MSO-Neurons

Additional to the correlations between morphological measures and physiological properties (Fig. 4.7), I investigated the morphological symmetry of the lateral and medial dendritic tree for each morphology. I found significant asymmetries in volume, surface area, and total cell length for both age groups, *mature ages* and *all ages* (Fig. 4.8A,B). All these measures are larger in the lateral dendritic trees (Table 2.1). Together with results depicted in Figure 4.7, it turns out that *total cell length* is an

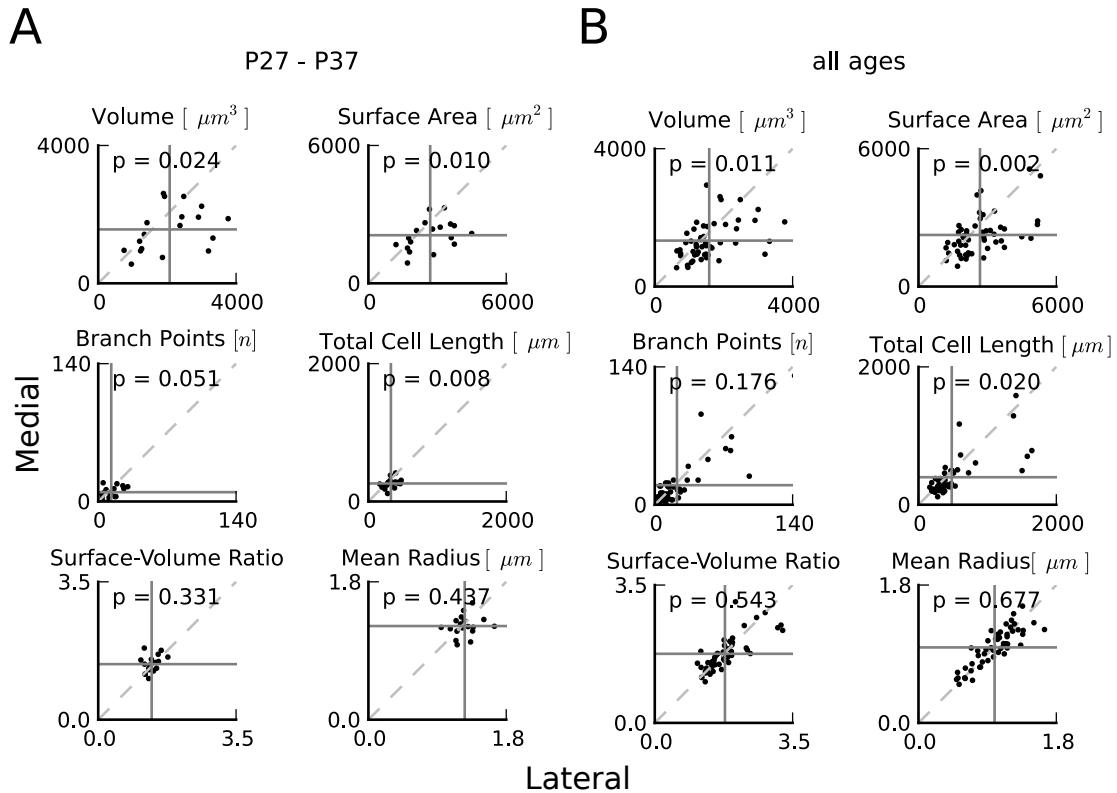


Figure 4.8: Morphological symmetry. Morphological properties of the lateral and medial dendritic tree with respect to *volume*, *surface area*, *branch points*, *total cell length*, *surface-volume ratio*, and *mean radius* (A: P27-P37, mature ages, B: all ages). *Volume*, *surface area*, and *total cell length* show a significant lateralization for both age groups, exposing the lateral dendrite.

informative measure: it correlates the most with M_τ and M_R being at the same time significant asymmetric towards the lateral dendritic tree.

I next investigated the electrophysiological effect of morphology on lateralized synaptic input. I asked whether the dendritic integration is symmetric or asymmetric for the medial and lateral dendritic tree. In order to compare the dendrites, I kept the conductance constant at 3 mS/cm^2 and axial resistivity constant at $80 \Omega \cdot \text{cm}$ for all morphologies. Synapses were placed in each morphology across one entire dendritic tree (Fig. 4.9A, illustration). The conductance of each synapse was taken such that the total conductance per branch was 100 nS for all models. The synapses were stimulated simultaneous, and the voltage response was recorded at the soma. I took four electrophysiological measures for the voltage response to the stimulation of one dendrite (Fig. 4.9A):

- *amplitude*: $V_{\max} - V_{\text{rest}}$
- t_{20-80} : time of changing from 20% to 80% of the maximal change of the voltage
- t_{exp} : time of changing from 100% down to 37% of the maximal change of the voltage
- *delay*: time to reach V_{\max} after stimulus onset

I found a lateralization for t_{20-80} and for *delay* within age group *mature* (Fig. 4.9A, P27-P37), where both values are larger at the lateral dendritic trees compared to the medial one. None of the other conditions reflect a significant lateralization of the response for any age group.

After comparing the lateral and medial dendritic tree with these measures, I looked how the values change across age. In contrast to variability of the morphological properties shown in chapter three, or Figure 4.6C, I find that *delay*, t_{20-80} , and t_{exp} do not change across age (Fig. 4.10A-C). The *amplitude* of the voltage response at the soma, however, increases with age (Fig. 4.10D). This indicates that with age the effect of dendritic attenuation decreases and is in line with results shown in Figures 3.3, 3.4, and 4.6A,B that show a punctification of morphology with age.

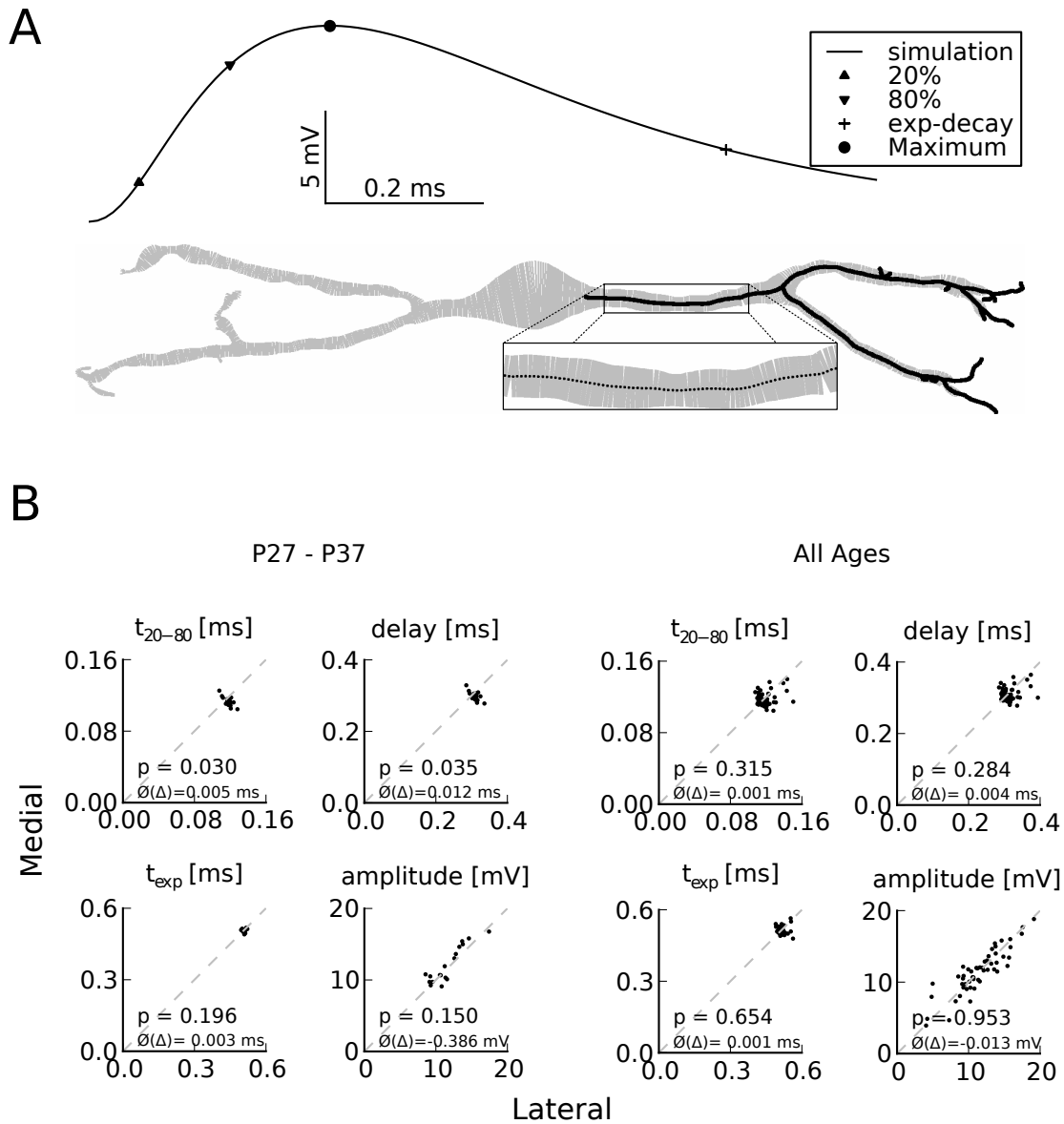


Figure 4.9: Electrophysiological symmetry. **A:** Alpha-synapses were equally distributed across the lateral or medial dendritic tree with a total conductance of $0.1 \mu\text{S}$ and time constant of $\tau_{\text{syn}} = 0.1$ ms. All synapses were activated at the same time. The resulting voltage was measured at the center of the soma, fitted, and the fit analyzed for t_{20-80} (time between triangles), t_{exp} (time between circle and cross), *delay* (time of circle), and *amplitude* (voltage difference between initial value and the maximum). **B:** Comparison of responses to lateral and medial synaptic stimulation grouped for two different age-groups (P27–P37: *mature ages*; P9–P37: *all ages*). Each dot represents the response of one morphology after lateral (x-axis) and medial (y-axis) synaptic stimulation, showing t_{20-80} , t_{exp} , *delay*, and *amplitude* (from top to bottom) of the voltage response. For *mature ages*, t_{20-80} and *delay* show significantly higher values for lateral dendritic trees.

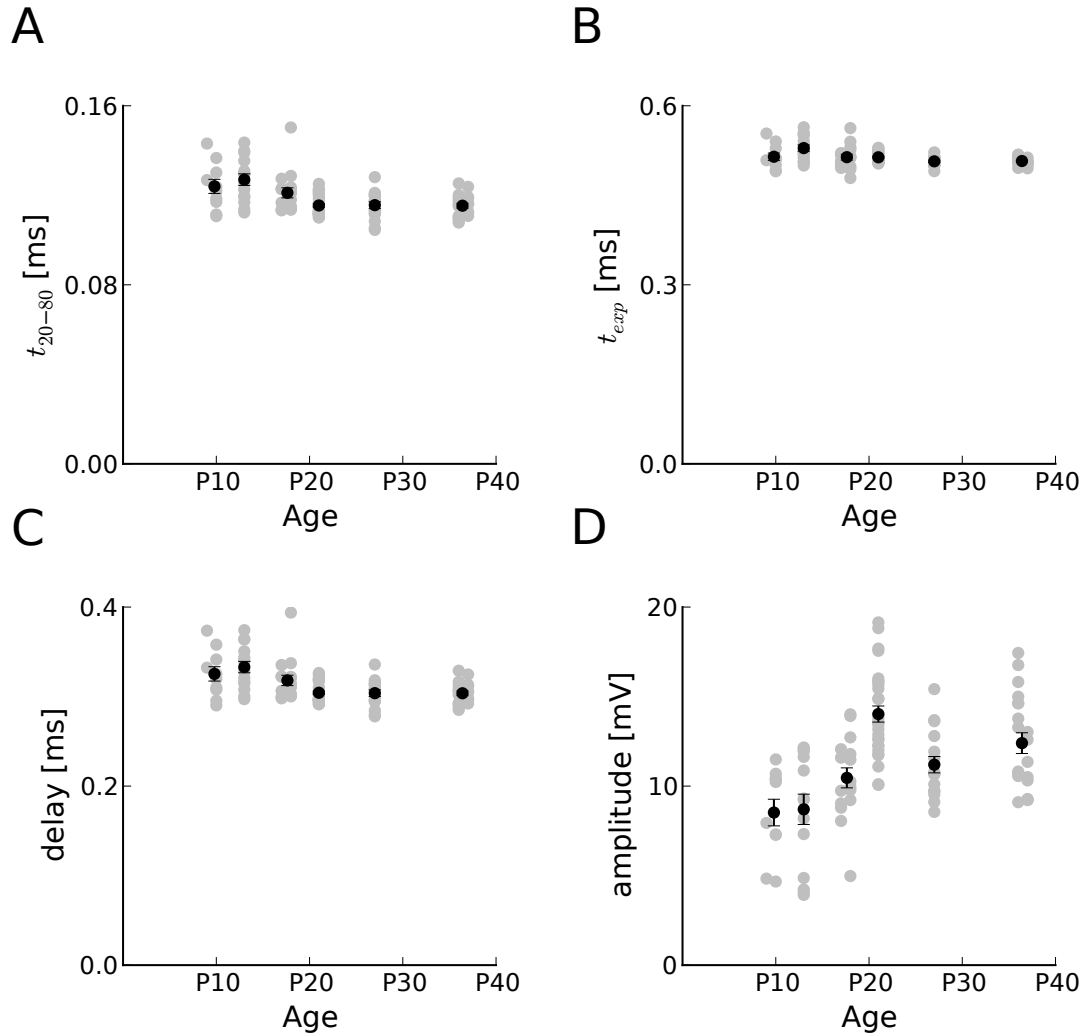
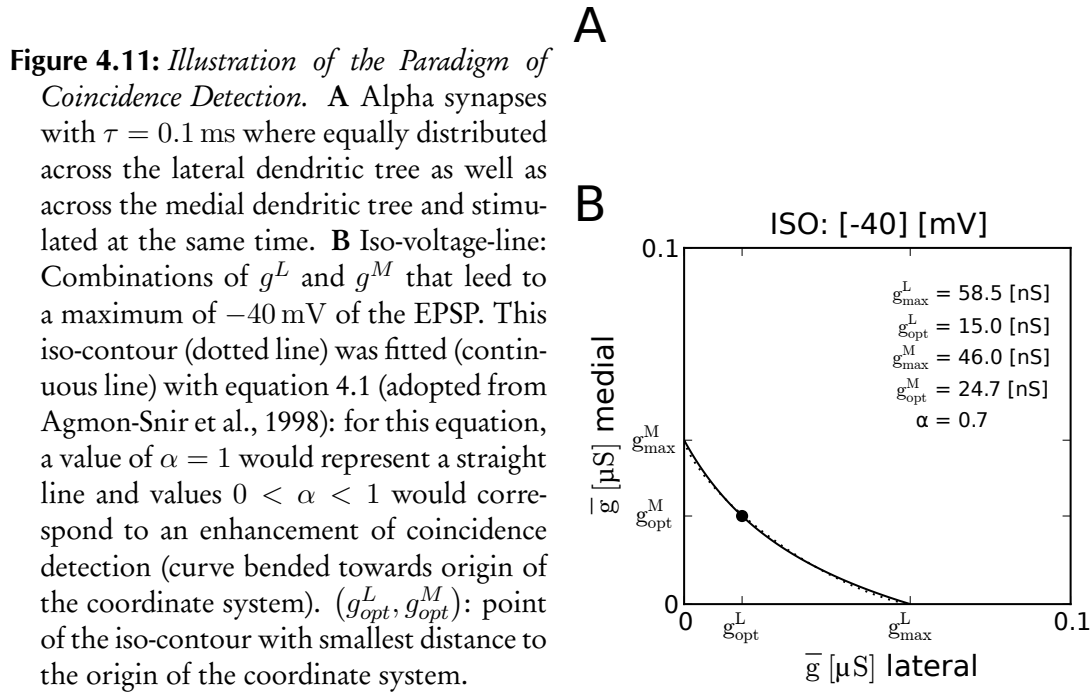


Figure 4.10: *Development of Electrophysiological Properties.* (Values of Fig. 4.9B as function of age) **A-C:** The measures t_{20-80} -time (A), decay time (B), and *delay* (C) do not change across age. **D:** The *amplitude* of the voltage response at the soma increases with age. **Color code:** Gray dots represent individual morphologies; black dots represent average values of a given age group according to Table 2.1.



4.6 Coincidence Detection

MSO neurons are sensitive to interaural time differences (ITDs) by performing a coincidence detection of the bilateral excitatory inputs. Therefore, I also investigated the role of the shape of dendrites for coincidence detection. As we already saw in Figure 4.2A, morphology influences passive properties of the neuron in a non-linear way. In order to quantify the enhancement of coincidence-detection properties, I used the concept of conductance threshold to explain the gain of coincidence-detection capabilities.

Using synaptic inputs distributed equally across each dendritic tree (Fig. 4.11) and applying variable total conductances for the medial (\bar{g}^M) and lateral (\bar{g}^L) dendritic tree, I measured the voltage response to simultaneous synaptic stimulation at the soma. The curve represents combinations of synaptic conductances which lead to a peak voltage response of the potential spike threshold of -40 mV at the soma (Fig. 4.11B). If these thresholds curves are bended towards origin of the coordinate system, coincidence-detection properties are enhanced: the threshold conductance

for the medial (g_{max}^M) and lateral (g_{max}^L) dendritic tree alone are bigger than optimal bilateral threshold conductances ($\bar{g}_{opt}^M + \bar{g}_{opt}^L$).

I found that integration of bilateral input was overall enhanced (Fig. 4.12A: each curve represents a single morphology. Note: all curves are bended towards origin). This indicates that the morphology of MSO-neurons enhances the coincidence-detection properties of the neuron which was also shown for morphologically simple models (Agmon-Snir et al., 1998; Dasika et al., 2007). I calculated the maximal gain of optimal lateralized input by dividing the sum of the optimal combination of total thresholds ($g_{opt}^M + g_{opt}^L$) by the minimum of the threshold conductance of the medial and lateral dendritic tree ($\min(g_{opt}^M, g_{opt}^L)$). I found that the mean gain over lateralized input was constantly about 20% for all ages (Fig. 4.12B).

Next, I analyzed how the dendritic trees attenuate the voltage response at the soma by calculating optimal total bilateral conductances ($g_{opt}^M + g_{opt}^L$) needed for reaching the threshold of -40 mV. This sum decreases from $0.075 \mu\text{S}$ at P9/10 to $0.05 \mu\text{S}$ at P36/37 (Fig. 4.12C, assuming fixed g_{rest}), indicating that the impact of synapses increases with age (see Figure 4.10D where the peak voltage response at the soma for fixed inputs increases with age).

To quantify the magnitude of coincidence enhancement by the dendritic trees, I adopted an approach by Agmon-Snir et al. (1998). The iso-voltage-contour was fitted with the following function:

$$\bar{g}_{medial}^\alpha = (g_{max}^L)^\alpha - \left(\frac{\bar{g}^L \cdot g_{max}^M}{g_{max}^L} \right)^\alpha \quad (4.1)$$

A value of $\alpha = 1$ represents a straight line and values $0 < \alpha < 1$ correspond to enhancement of coincidence detection (“curve bended towards origin”). This analysis confirmed that the dendritic trees enhance the coincidence-detection properties of MSO neurons (for all morphologies: $\alpha < 1$). However, this enhancement decreases during development (Fig. 4.12D: $\alpha = 0.6$ for P9/10 and $\alpha = 0.75$ for P36/37) which, again, corresponds to my finding of “punctification” of the neuron during development. I confirmed that dendritic morphology improves coincidence detec-

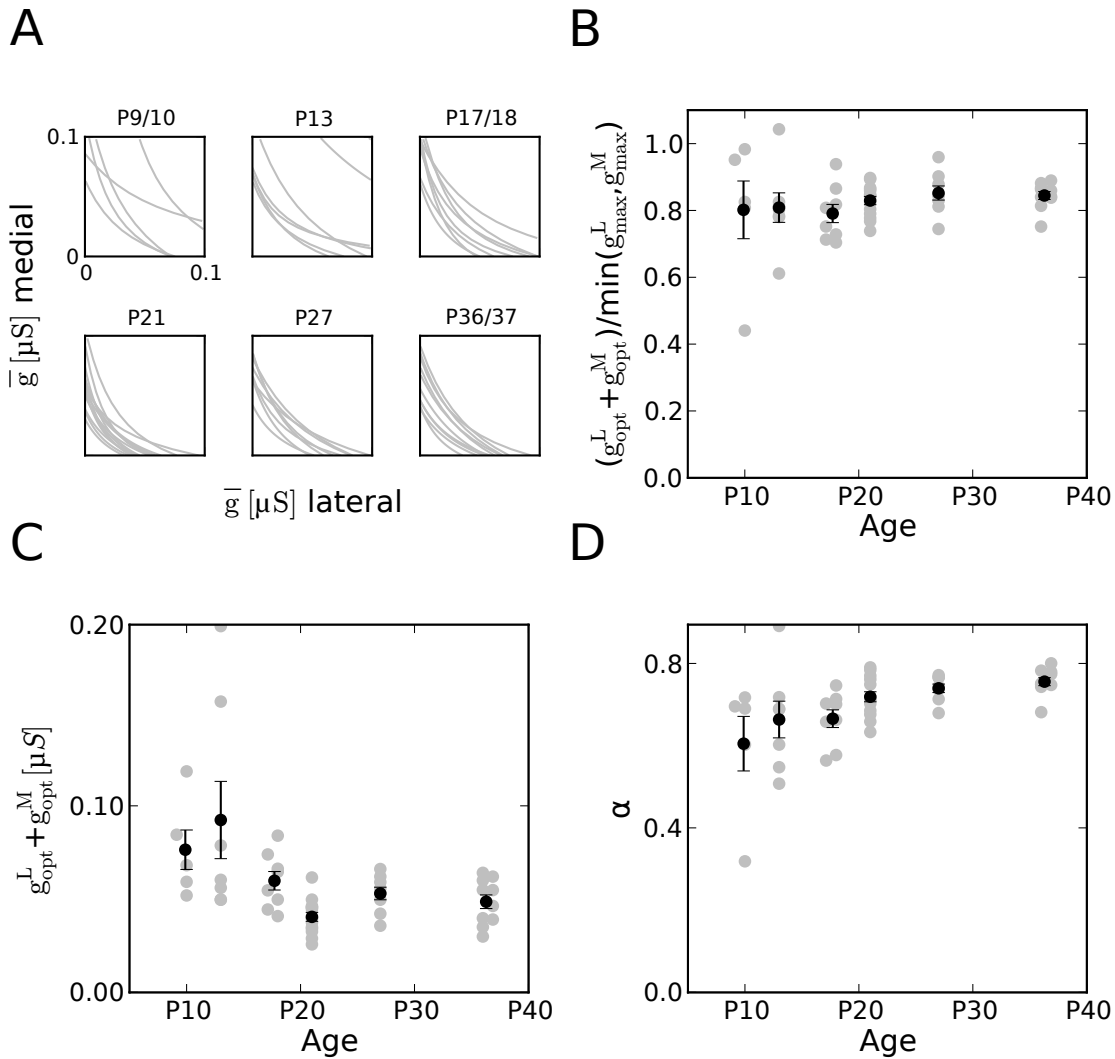


Figure 4.12: Morphological influence on coincidence detection. **A:** Iso-lines of all 52 morphologies grouped by age. All lines are bended towards the origin of the coordinate system. **B:** Relative binaural conductances a function of age (gray dots representing each morphology). The mean gain of lateralized input is constant $\sim 20\%$ across all ages. **C:** Minimal binaural conductances as a function of age. With increasing age the required sum conductance decreases to almost by 50%. **D:** Enhancement of coincidence detection: α (definition see A2) as a function of age. This analysis confirmed that the dendritic trees enhances the coincidence-detection properties of MSO neurons (for all morphologies: $\alpha < 1$). However, this enhancement decreases during development ($\alpha = 0.6$ for P9/10 and $\alpha = 0.75$ for P36/37). **Color code, B–C:** Gray dots represent individual morphologies; black dots represent average values of a given age group according to Table 2.1.

4 Electrophysiological Properties, Symmetry, and Coincidence-Detection-Characteristics

tion in accordance with the literature (Agmon-Snir et al., 1998; Dasika et al., 2007). However, early development rather weakens this effect.

5 Discussion

In my thesis, I analyzed two main morphological aspects of neurons of the medial superior olive (MSO) in detail: on the one hand, I metrically quantified their shapes with newly developed methods. On the other hand, I looked at the morphological impact on basic electrophysiological measures, at morphological symmetry, and at morphological properties of coincidence detection. As an animal model I used Mongolian gerbils (*Meriones unguiculatus*) during the late phase of postnatal development (P9 – P37). This period of time is of special interest, as it spans from just before hearing onset at P12-P13 (Finck et al., 1972; Ryan et al., 1982; Smith and Kraus, 1987) to adulthood.

Concerning the shape, I found that maturation was completed around P27, when the MSO neurons appeared morphologically compact and cylinder-like. I described a reduction of the dendritic arbor between P9 and P21, including a reduction in number of branch points, the total cell length, and the amount of cell membrane. The dendritic radius increases until P27 and is likely the main source of the increase in cell volume. In addition, I showed that in more than 85% of all MSO neurons, the axonal origin was located on the soma.

I used reconstructed morphologies of the first part of my thesis for multi-compartmental modeling. For these morphologies I estimated in a first step passive parameters according to published electrophysiological data of MSO neurons (Magnusson et al., 2005; Scott et al., 2005). In order to fit the axial resistivity of MSO neurons of adult gerbils, I developed a new method that accounts for the MSO-specific characteristics of a fast effective membrane time constant (τ_{eff}) around 0.3 ms in combination with very low input resistance (R_{in}) around 7 M Ω . Next, I demonstrated that morphological properties correlate with R_{in} and with τ_{eff} . Then I compared metric

and electrophysiological properties of the medial and lateral dendritic tree of each reconstructed morphology. Finally, I investigated properties of coincidence detection of morphologies of MSO neurons.

I will discuss that these findings are of interest with respect to MSO specific research but also with respect to other areas of neuroscience. Here, I would like to take methodological aspects into account as well as to discuss the impact of morphologies in general.

5.1 New Findings on Properties of Neurons of the MSO

5.1.1 MSO-Morphologies Improve Coincidence Detection

MSO neurons are sensitive to ITDs by performing a coincidence detection of the bilateral excitatory inputs (for review see Grothe et al., 2010). One aspect of this task is the dendritic information processing that underlies auditory coincidence detection. Various studies explored this aspect by using simplified multi-compartmental models. These models could demonstrate that dendrites enhance bilateral integration and improve coincidence detection beyond that expected from *point neurons* (Agmon-Snir et al., 1998; Zhou et al., 2005; Dasika et al., 2007). “The biophysical mechanism for this improvement is based on the nonlinear summation of excitatory inputs in each of the dendrites and the use of each dendrite as a current sink for inputs to the other dendrite” (Agmon-Snir et al., 1998). However, biological detailed models at different stages of development were still missing.

I explored coincidence characteristics of MSO morphologies by simulating equally distributed synapses across each dendrite. I showed that the biological shape of MSO neurons enhances coincidence detection. However, this *enhancement by morphology* decreases with age (Fig. 4.12D). Although being contra intuitive – as coincidence detection is considered to be a primary task of this type of neuron – this development is in line with my metric findings. Here, during the investigated period of time,

surface area reduces, surface-volume-ratio increases, total cell length decreases, and dendrites become thicker. In addition, the modulation index of both R_{in} and τ_{eff} decreases with age. All of these changes (Figs. 3.3, 3.4, and 4.6A,B) indicate that the dendritic impact on signal processing decreases.

5.1.2 Development of MSO-Morphologies After Hearing Onset

I quantified the developmental changes of the dendritic arbor and cell architecture in the gerbil MSO between P9 and P37. Recent findings suggested that for neurons in the gerbil MSO, the reduction of small dendritic protrusions occurred predominantly during early postnatal development, up to P12 (Chirila et al., 2007). This finding is in contrast to reports obtained from rat and gerbil MSO and lateral superior olive (LSO) illustrating that loss of small dendritic protrusions continues after hearing onset (Rogowski and Feng, 1981; Sanes et al., 1992a; Rietzel and Friauf, 1998). Similar to these latter reports, I found that the refinement of the dendritic arborization, including the retraction of small branches, lasts until at least P21. The difference between our study and work by Chirila et al., 2007 might be caused by counting different branch categories. Here, I did not discriminate between branch and protrusion types because our metric information did not provide an appropriate criterion for such a categorization (Fig. 3.5). In general, the decrease in the number of small branches and, thereby, the number of branch points was matched by a reduction in total cell length and surface area of the cell. The relative reduction of branch points was largest at the proximal dendrites; thus the remaining branches were located more distally (Fig. 3.2). The functional consequence of the remaining branches being located on more distal dendritic regions is unknown.

I also observed that the cell volume increased until P27 (Fig. 3.3). Such an increase in the cell volume could be largely explained by a twofold increase in dendritic diameter (Fig. 3.4) that developmentally coincided with the increase in cell volume. However, somatic morphology can not be accounted for this increase in cell volume. Its size stays constant during the investigated period (Fig. 3.1).

Together, the overall developmental alterations continued after hearing onset and lasted until P27, finally generating a morphologically compact, cylinder-like MSO neuron. The developmental time course described here is in agreement with electrophysiological findings by Scott et al. (2005). These authors found that electrophysiological parameters such as input resistance, the shape of the action potential, and the shape of the excitatory postsynaptic potential changed most between P14 and P20. However, full maturation of these electrophysiological responses was found only between P25 and P30.

By comparison, in the avian analog structure the nucleus laminaris (NL), a dendritic refinement was apparent during later stages of the development, where it was found that the number of dendrites and branches were reduced. For the NL, this holds not only for the higher order branches, but also for primary dendritic branches (Smith, 1981). In contrast, I found that the number of main MSO dendrites remained unchanged. Therefore, the pattern of dendritic refinement appears to be different in the MSO and NL.

5.1.3 Estimating Passive Parameters of Models of MSO neurons

In the present thesis, I explored biophysical properties and the effects of dendrites in complex, multi-compartmental neuron models of auditory coincidence-detector cells. Each multi-compartmental model is composed of up to several thousand compartments, describing the morphology of MSO cells with their soma, lateral dendrite, and medial dendrite in high detail.

Using the morphologies reconstructed in the first part of my thesis, I first confirmed the general impact of morphology on R_{in} and τ_{eff} . Theoretically, it exists an optimal axial resistivity that minimizes effective time constant for a given morphology with constant membrane conductance and specific membrane capacity. The fast information processing of the MSO takes advantage of this effect as I showed in chapter four.

Input resistance and effective membrane time constant of MSO neurons reach for adult animals an asymptotic value of about $7\text{ M}\Omega$ and 0.3 ms , respectively (Scott et al.,

2005). Using these data, I fitted an axial resistivity of $\varrho = 80 \Omega \cdot \text{cm}$ and a total membrane conductance at resting potential of $g_{\text{rest}} = 3 \text{ mS}/\text{cm}^2$ for the reconstructed subset of cell morphologies. My estimation of the axial resistivity differs from $200 \Omega \cdot \text{cm}$ that was used in previous studies for computational models (Svirskis and Rinzel, 2000). The general conclusions drawn by these authors wouldn't be affected. However, it has an impact on specific quantifications, as lower axial resistivity changes the influence of the morphological shape to electrophysiological properties of the cell. The dendritic effect decreases and the behavior of the model modifies toward a behavior of the *surface-equivalent* point neuron¹.

5.1.4 The Influences of Activity on MSO-Morphologies

My data show that cellular refinement continues after hearing onset. Thus, auditory cues other than spontaneous background activity might affect the morphology of MSO neurons. This suggests that functional needs might play a role in adjusting the final cell architecture. That auditory activity other than background is needed for proper adjustment of the MSO inputs has been suggested based on electrophysiological in vivo (Seidl and Grothe, 2005) and in vitro recordings (Magnusson et al., 2005), as well as immunohistochemistry (Kapfer et al., 2002) and input tracing (Werthat et al., 2008). These studies, however, focused on the input pattern, rather than the morphology of the MSO neuron itself. Our finding that morphological maturation was accomplished between P20 and P30 and hence might be activity-dependent is in line with findings that describe a similar developmental time course of the maturation process in gerbil LSO neurons (Sanes et al., 1992a). Unilateral sound deprivation altered the development of the LSO dendritic morphology (Sanes et al., 1992b), and the size of the dendritic arbor appeared to correlate with the tonotopic gradient of the LSO (Sanes et al., 1990). It can be speculated that binaural activity is also involved in the maturation of MSO neurons in gerbils as described here. In this light, it would

¹*Surface-equivalent*: Equivalent with respect to surface area. In terms of modeling: simulations with either detailed model but $\varrho = 0$, or spherical model without morphology with identical surface area as the detailed model.

be of interest to know when the maturation of ITD functions is fully accomplished. Behavioral experiments showed that gerbils are capable of detecting azimuthal sound sources at P20, although with low precision (Kelly and Potash, 1986). Possibly, the late dendritic refinement described between P20 and P27 is needed for the high precision in detecting azimuthal sound sources observed in adult animals (Maier et al., 2008).

5.1.5 Morphological Assymetries and its Implications

Asymmetry appears on different levels within the system of processing interaural time differences (ITDs). The peripheral level of asymmetry is the neural circuit from the auditory nerve (AN) to the MSO that I described in chapter 1.3. Here, Jercog et al. (2010) showed that the delays to peak of contralateral responses were on average about $500 \mu\text{s}$ longer than those of ipsilateral responses on the same recorded neuron. In their paper, they discuss circuit properties that may influence the asymmetric delay, like an asymmetric vector strength of monolateral presynaptic inputs. However, it has to be considered that these findings are based on experiments using brain slices and are not confirmed by in vivo experiments.

The aspect of the present thesis is the asymmetry of a MSO neuron itself, and how such an asymmetry influences ITD-processing. On the cellular level, the idea of axonal displacement was already investigated by Zhou et al., 2005. The location of the axonal origin is thought to be of functional significance. Theoretical considerations led to the suggestion that a dendritic axonal origin is important for ITD tuning of MSO neurons (Brew, 1998; Zhou et al., 2005). It was hypothesized that if the axon is located on a dendrite, it would lead to an asymmetrical input output distance for the two main dendrites. This asymmetry would generate an imbalance between the ipsilateral and contralateral excitatory inputs. Based on this asymmetry, Zhou et al., 2005 established a model that explains tuning to physiologically relevant ITDs. They demonstrated an ITD coding that relied on a location of the axon on the lateral dendrite at a distance of $45 \mu\text{m}$ to the soma. With their model, this displacement leads to a transfer delay difference between contralateral and ipsilateral

excitations in the passive condition of $\sim 350 \mu\text{s}$ (which would add to the delay difference mentioned above). However, here we showed that at least 85% of all detected axons originate on the somatic region of neurons in the gerbil MSO. This finding confirms earlier suggestions that, in gerbils, the axons originate from the MSO soma (Kuwabara and Zook, 1999; Scott et al., 2005), similar to the cells in the avian analog structure, the NL (Kuba et al., 2006). Our findings contrast with evidence obtained from guinea pig (Smith, 1995) and cat (Kiss and Majorossy, 1983). One explanation for the different findings could simply be based on differences in the analysis. The three-dimensional analysis used in the present thesis is not susceptible to perspective distortion compared to two-dimensional analyses used in earlier studies.

In contrast to an asymmetric displacement of the axon origin, a comparison of lateral and medial dendritic trees of MSO neurons, however, was still missing. Here, I focused on the asymmetry of the shape of single neurons of the MSO as well as on the asymmetry of the passive electrophysiological properties of their dendritic trees. As a result, volume, surface area, and total cell length are significantly asymmetric for both age groups, *mature ages* and *all ages* (Fig. 4.8A,B). Moreover, all these measures are larger in the lateral dendritic trees. These results explain also – under symmetric *peripheral* conditions – that synaptic input is processed asymmetrically: the mature lateral dendrite has a stronger delay of $\sim 12 \mu\text{s}$ and a longer rise time of ($\sim 5 \mu\text{s}$) than the medial dendrite (Fig. 4.9B). Although being on a smaller scale, this difference counteracts both asymmetries mentioned above: dendritic delay of contralateral excitation at MSO neurons is smaller compared to ipsilateral excitation. For future investigations it would be interesting to see how *asymmetries* interact. Here, models should also implement active properties of the dendritic membrane (Mathews et al., 2010).

5.2 Widening the View: Implications on Other Areas

5.2.1 Transformation of Brain Tissue Modifies the Neurons Shape During Methodological Procedures

Brain tissue is known to shrink when exposed to paraformaldehyde during the fixation process, and mounting brain slices between coverslips imposes pressure on the tissue, leading to flattening. I analyzed both shrinkage and flattening independently for brain slices from young (P9) and mature (P36) animals. I found that shrinkage appears to be less problematic than tissue flattening for a comparison between different age groups (see Materials & Methods, Chapter 2.4). To minimize the effect of tissue alterations, I normalized dimensions as for instance *distance from root* (Figs. 3.2, 3.4, 3.6). These normalizations are important, as I found a $\sim 25\%$ difference in the absolute dendritic extent between P9 and P37 that could be explained by the difference in measurement-induced tissue alterations. The different tissue alterations led to an overestimate of the changes in the total length of the cell and amount and distribution of surface area of the cell (Figs. 3.3D, 3.6), whereas the increases in the average of the terminal length, the cell volume, and the dendritic radius (Figs. 3.3C,E, 3.4) were underestimated. Because the changes in average of the terminal length (Fig. 3.3C) were underestimated and the total length of the cell was overestimated, the change in the number of terminal compartments (Fig. 3.2) appeared balanced by the two effects.

Concerning the present study, the alterations caused by tissue shrinkage and flattening did not substantially influence the finding that MSO neurons become more compact during postnatal development, nor that the axon originates from the soma region. However, I could demonstrate that brain tissue modifies its metric properties by the experimental procedure. The extend of this modification depends on the age of the tissue, presumably on the brain region, and on the experimental fixation and mounting procedure. This has to be taken into account especially when models are build exclusively on metric information.

5.2.2 Reducing Complexity of Detailed Multi-Compartmental Models and Mapping Functions Onto Neuronal Morphology

Simulations of detailed multi-compartmental models of MSO neurons show different results than simulations of their *surface-equivalent* point neurons. In order to quantify this influence assuming the estimated passive values, I introduced one modulation index for input resistance (M_R) and one for effective membrane time constant (M_τ) which compares models of our simulation paradigm with their *surface-equivalent* point neuron. With these modulation indices I could show that the morphology changes during development in a way that its impact decreases, the neurons *punctify*. This goes in line with my metric analysis (Figs. 3.3 and 3.4). However, these developmental changes of morphology have their limits in explaining all findings in the literature. For instance the strong increase of input resistance during early development (Magnusson et al., 2005; Scott et al., 2005) can not be explained by the influence of morphological changes. Here, I showed that the membrane conductance increases about 15 fold between P10 and P21.

How does the described morphological impact correlate with specific metric properties of the morphology? I showed that during the entire investigated period (including strong developmental alterations between P9 and P27) surface-volume-ratio, total cell length, mean radius, and number branch points correlate most with M_R and M_τ – and not surface area or volume (Fig. 4.6A,B). This has implications for choosing an appropriate method to reduce the numbers of compartments of a detailed model to functional groups of compartments. This reduction of parameter space in order to decrease complexity (and simulation time), but also in order to investigate morphological core properties that map functions onto neuronal morphology (Stiefel and Sejnowski, 2007). The constraint of preserving surface area which is applied in several methods (Tobin et al., 2006) should, therefore, be adjusted. For the MSO, e.g. total cell length should be taken into account, as this measure correlates most with M_R and M_τ , and is also significantly asymmetric for its medial and lateral dendritic tree (Figs. 4.7, 4.8).

Also, a method that reduces morphological complexity should make use of electrophysiological properties of a neuron. In the same way that I took advantage of a fast effective membrane time constant in combination with a low input resistance in order to fit ϱ (Fig. 4.5), electrophysiological characteristics can be used determining a simplified morphology. As for the MSO, one approach could start with the following conditions for a simplified model: three compartments, where two identical represent one dendrite and one represents the soma. This soma has a geometry of $27\ \mu\text{m}$ in length and $13\ \mu\text{m}$ as diameter (according to Fig. 3.1). Fixed parameters would be set to $g_{\text{rest}} = 3\ \text{S}/\text{cm}^2$ and $\varrho = 80\ \Omega\cdot\text{cm}$. Then, the two geometric parameters of the dendritic compartment length and diameter could be determined in a way that the resulting morphology would fit $R_{\text{in}} = 7\ \text{M}\Omega$ and $\tau_{\text{eff}} = 0.3\ \text{ms}$. Similarly, this approach could change the way detailed reconstructions of diverse types of neurons are mapped to simplified models. With increasing amount of electrophysiological data that is available, there is no reason to keep surface area as the dominant reference magnitude to simplify models. In contrary, taking electrophysiological data into account simplifying complex models will capture properties of a neuron more realistically. Also, the resulting parameters of the simplified model can offer valuable clues to the morphological core properties that map functions onto neuronal morphology.

5.2.3 Morphologies Implement Diverse Arborization Patterns

Most neurons have dendritic trees that receive many excitatory and inhibitory synaptic inputs. Arborization patterns of a dendritic trees influence the way how synaptic events are integrated. These arborization patterns differ for varying types of neurons adjusting dendritic integration of synaptic inputs to their role within the nervous system. As for instance, dendritic arborization of pyramidal neuron regulates strongly coincidence detection of inputs arriving from different cortical layers which provides a mechanism by which structural plasticity can change the rules for dendritic integration of multilayer synaptic input to neocortical cells (Schaefer et al., 2003). Here, structural plasticity and coincidence detection are associated with learning (*cells that*

fire together wire together, Hebbian theory). Also, dendritic architecture determines the degree of passive normalization of synaptic integration. Compared to CA1 pyramidal neurons, dendritic trees of CA3 interneurons, CA3 pyramidal neurons, and dentate granule cells normalize synaptic inputs to a high degree (Jaffe and Carnevale, 1999). These findings can also be seen in neurons of insects. Dendrites of lobula plate tangential cells of the fly's visual system integrate visual motion information over a large array of columnar elements arranged retinotopically as a spatial map (Borst and Haag, 2002). Again, the current transfer from all dendritic locations to the axonal summation point is strongly equalized throughout the dendrite (Cuntz et al., 2007). However, underlying optimization principles described by Cuntz et al., 2007 seem not to be realized for dendritic architecture of neurons of the MSO: dendritic diameter tapering (see Fig. 3.4) cannot be characterized by a quadratic fit. In contrary, the tube-like shape of primary dendrites favors substantial location-dependent variability of somatic postsynaptic potential amplitude (Jaffe and Carnevale, 1999). Moreover, a thick and tube-like dendrite decreases the resistance between distal synapses and the soma. This mechanism might reduce dendritic attenuation and thus keep the somatic input caused by synaptic events effective in spite of their metric segregation according to the site of aural stimulation.

5.3 Conclusion

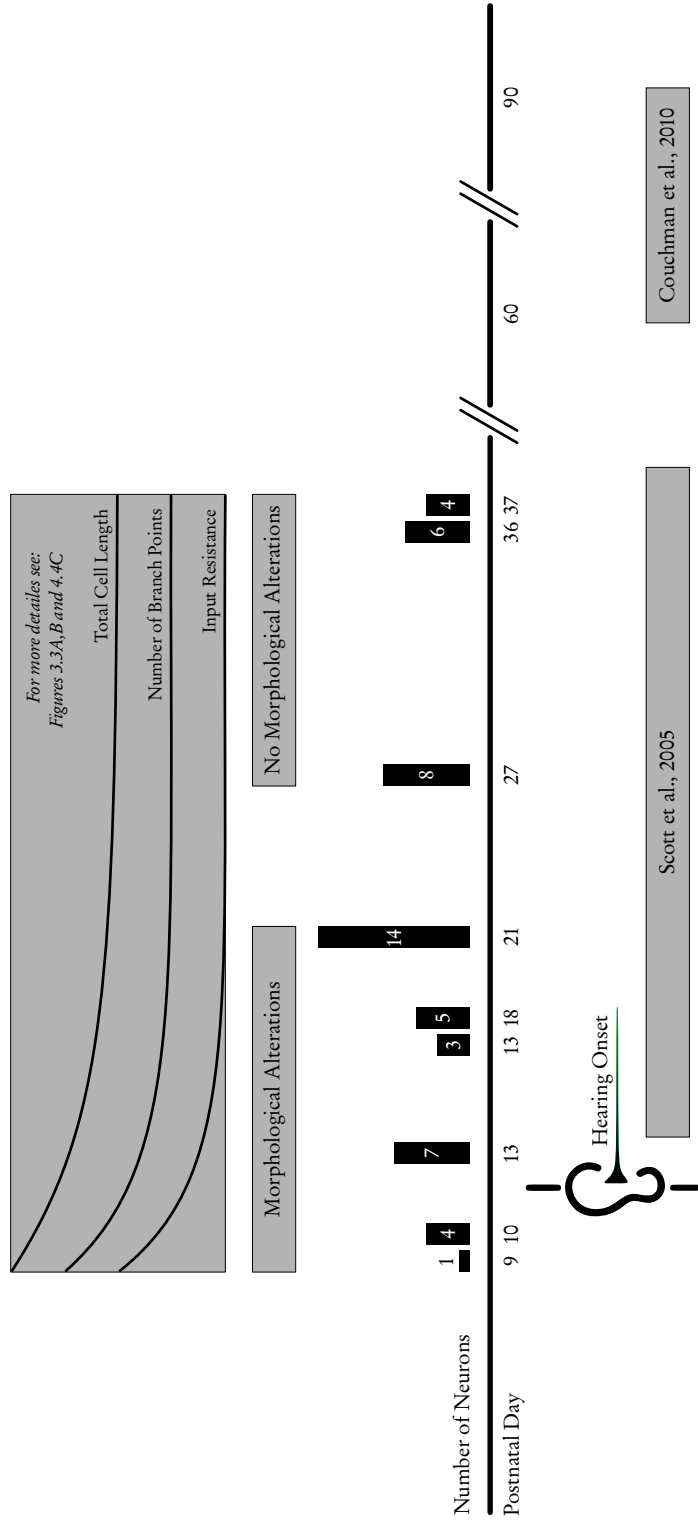
Sound localization in the azimuthal plane challenges its processing neural circuits. Evolution developed highly specialized neurons that are integrated into these neural circuits. Here, depending on the functional role and the stage of development, neural morphology shows specific characteristics.

In the present thesis, I provide a detailed quantification of morphologies of neurons of the MSO during late postnatal development. Moreover, I used the detailed morphological information to build multi-compartmental models in order to demonstrate the impact of neural shape of MSO neurons on electrophysiology. It could be confirmed that morphology of passive dendrites influences coincidence detection. This fundamental role was already investigated looking at diverse types of neurons that are part of different neural circuits. This demonstrates that coincidence detection is a general computational principle that contributes to diverse tasks of neurons and neural circuits.

More analyses would be necessary to further elucidate neural mechanisms underlying coincidence detection. The possibility is that this would enable scientists to generate other *computational building blocks* (Agmon-Snir et al., 1998) that, in consequence, might help to deeper understand of coincidence detection – not only as a part of coding interaural time difference but also as a general computational principle.

6 Appendix

6.1 Timeline



Bibliography

- Adams, J. C. (1979). Ascending projections to the inferior colliculus. *The Journal of Comparative Neurology*, 183(3):519–538.
- Adams, J. C. and Mugnaini, E. (1990). Immunocytochemical evidence for inhibitory and disinhibitory circuits in the superior olive. *Hearing Research*, 49(1-3):281–298.
- Agmon-Snir, H., Carr, C. E., and Rinzel, J. (1998). The role of dendrites in auditory coincidence detection. *Nature*, 393(6682):268–272.
- Batteau, D. W. (1967). The role of the pinna in human localization. *Proceedings of the Royal Society of London. Series B. Biological Sciences*, 168(1011):158–180.
- Beckius, G. E., Batra, R., and Oliver, D. L. (1999). Axons from anteroventral cochlear nucleus that terminate in medial superior olive of cat: observations related to delay lines. *The Journal of Neuroscience*, 19(8):3146–3161.
- Bialek, W. and Zee, A. (1990). Coding and computation with neural spike trains. *Journal of Statistical Physics*, 59(1-2):103–115.
- Borst, A. and Haag, J. (2002). Neural networks in the cockpit of the fly. *Journal of Comparative Physiology A: Neuroethology, Sensory, Neural, and Behavioral Physiology*, 188(6):419–437.
- Brand, A., Behrend, O., and Grothe, B. (2002). Precise inhibition is essential for microsecond interaural time difference coding. *Nature*, 417:543–547.

- Brew, H. M. (1998). Modeling of interaural time difference detection by neurons of mammalian superior olivary nucleus. *Association for Research in Otolaryngology*, 25:680.
- Cajal, R. Y. (1909). *Histologie du Systeme Nerveux de L'Homme et des Vertebres. Generalites, Moelle, Ganglions Rachidiens, Bulbe & Protuberance. Maloine, Paris.*
- Carr, C. E. and Konishi, M. (1990). A circuit for detection of interaural time differences in the brain stem of the barn owl. *The Journal of Neuroscience*, 10(10):3227–3246.
- Chirila, F. V., Rowland, K. C., Thompson, J. M., and Spirou, G. A. (2007). Development of gerbil medial superior olive: integration of temporally delayed excitation and inhibition at physiological temperature. *Society*, 1:167–190.
- Clark, G. M. (1969). The ultrastructure of nerve endings in the medial superior olive of the cat. *Brain Research*, 14(2):293–305.
- Coleman, P. D. (1963). An analysis of cues to auditory depth perception in free space. *Psychological Bulletin*, 60(3):302–315.
- Couchman, K., Grothe, B., and Felmy, F. (2010). Medial Superior Olivary neurons receive surprisingly few excitatory and inhibitory inputs with balanced strength and short-term dynamics. *Journal of Neuroscience*, 30(50):17111–17121.
- Covey, E. and Casseday, J. H. (1991). The monaural nuclei of the lateral lemniscus in an echolocating bat: parallel pathways for analyzing temporal features of sound. *The Journal of Neuroscience*, 11(11):3456–3470.
- Cuntz, H., Borst, A., and Segev, I. (2007). Optimization principles of dendritic structure. *Theoretical Biology and Medical Modelling*, 4:1–8.
- Curtis, H. J. and Cole, K. S. (1938). Transverse electric impedance of the squid giant axon. *The Journal of General Physiology*, 21(6):757–765.

- Dasika, V. K., White, J. a., and Colburn, H. S. (2007). Simple models show the general advantages of dendrites in coincidence detection. *Journal of Neurophysiology*, 97(5):3449–3459.
- Decharms, R. and Zador, A. (2000). Neural representation and the cortical code. *Annual Review of Neuroscience*, 23(1):613–647.
- Evers, J., Schmitt, S., Sibila, M., and Duch, C. (2005). Progress in functional neuroanatomy: precise automatic geometric reconstruction of neuronal morphology from confocal image stacks. *Journal of Neurophysiology*, 93(4):2331.
- Feng, a. S. and Rogowski, B. a. (1980). Effects of monaural and binaural occlusion on the morphology of neurons in the medial superior olivary nucleus of the rat. *Brain Research*, 189(2):530–534.
- Finck, A., Schneck, C. D., and Hartman, A. F. (1972). Development of cochlear function in the neonate Mongolian gerbil (*Meriones unguiculatus*). *Journal of Comparative and Physiological Psychology*, 78(3):375–380.
- Goldberg, J. M. and Brown, P. B. (1969). Response of binaural neurons of dog superior olivary complex to dichotic tonal stimuli: some physiological mechanisms of sound localization. *Journal of Neurophysiology*, 32(4):613–636.
- Grau-Serrat, V., Carr, C. E., and Simon, J. Z. (2003). Modeling coincidence detection in nucleus laminaris. *Biological Cybernetics*, 89(5):388–396.
- Grothe, B. (2003). New roles for synaptic inhibition in sound localization. *Nature Reviews Neuroscience*, 4(7):540–550.
- Grothe, B., Köppl, C., Casseday, J. H., and Carr, C. E. (2004). The evolution of central pathways and their neural processing patterns. In Manley, G. A., Popper, A. N., and Fay, R. R., editors, *Evolution of the Vertebrate Auditory System*, pages 289–359. Springer, New York.

- Grothe, B., Pecka, M., and McAlpine, D. (2010). Mechanisms of sound localization in mammals. *Physiological Reviews*, 90(3):983–1012.
- Gulledge, A. T., Kampa, B. M., and Stuart, G. J. (2005). Synaptic integration in dendritic trees. *Journal of Neurobiology*, 64(1):75–90.
- Henkel, C. and Brunso-bechtold, J. (1990). Dendritic morphology and development in the ferret medial superior olivary nucleus. *The Journal of Comparative Neurology*, 294(3):377–388.
- Hines, M. L. (1984). Efficient computation of branched nerve equations. *International Journal of Bio-Medical Computing*, 15(1):69–76.
- Hines, M. L. (1993). NEURON – a program for simulation of nerve equations. *Neural systems: Analysis and Modeling*, pages 127–136.
- Hines, M. L. and Carnevale, N. (2000). Expanding NEURON’s repertoire of mechanisms with NMODL. *Neural Computation*, 12(5):995–1007.
- Hines, M. L. and Carnevale, N. (2001). NEURON: a tool for neuroscientists. *The Neuroscientist*, 7(2):123.
- Hines, M. L., Davison, A. P., and Muller, E. (2009). NEURON and Python. *Frontiers in Neuroinformatics*, 3(1):1–12.
- Hudspeth, A. J., Choe, Y., Mehta, A. D., and Martin, P. (2000). Putting ion channels to work: mechano-electrical transduction, adaptation, and amplification by hair cells. *Proceedings of the National Academy of Sciences of the United States of America*, 97(22):11765–11772.
- Jaffe, D. B. and Carnevale, N. T. (1999). Passive normalization of synaptic integration influenced by dendritic architecture. *Journal of Neurophysiology*, 82(6):3268–3285.
- Jeffress, L. A. (1948). A place theory of sound localization. *Journal of Comparative and Physiological Psychology*, 41(1):35–39.

- Jercog, P. E., Svirskis, G., Kotak, V. C., Sanes, D. H., and Rinzel, J. (2010). Asymmetric excitatory synaptic dynamics underlie interaural time difference processing in the auditory system. *PLoS Biology*, 8(6):e1000406.
- Joris, P. X. and Smith, P. H. (2008). The volley theory and the spherical cell puzzle. *Neuroscience*, 154:65–76.
- Kapfer, C., Seidl, A., and Schweizer, H. (2002). Experience-dependent refinement of inhibitory inputs to auditory coincidence-detector neurons. *Nature Neuroscience*, 5(3):247–253.
- Kelly, J. B. and Potash, M. (1986). Directional responses to sounds in young gerbils (*Meriones unguiculatus*). *Journal of Comparative Psychology*, 100(1):37–45.
- Kiss, A. and Majorossy, K. (1983). Neuron morphology and synaptic architecture in the medial superior olivary nucleus. *Experimental Brain Research*, 52(3):315–327.
- Klumpp, R. G. and Eady, H. R. (1956). Some measurements of interaural time difference thresholds. *Journal of the Acoustical Society of America*, 28(5):859–860.
- Köppl, C. and Carr, C. E. (2008). Maps of interaural time difference in the chicken's brainstem nucleus laminaris. *Biological Cybernetics*, 98(6):541–559.
- Krichmar, J. L., Nasuto, S. J., Scorcioni, R., Washington, S. D., and Ascoli, G. a. (2002). Effects of dendritic morphology on CA3 pyramidal cell electrophysiology: a simulation study. *Brain Research*, 941(1-2):11–28.
- Kuba, H., Ishii, T. M., and Ohmori, H. (2006). Axonal site of spike initiation enhances auditory coincidence detection. *Nature*, 444(7122):1069–1072.
- Kubke, M. F., Massoglia, D. P., and Carr, C. E. (2004). Bigger brains or bigger nuclei? Regulating the size of auditory structures in birds. *Brain, Behavior and Evolution*, 63(3):169–180.
- Kulesza, R. J. (2007). Cytoarchitecture of the human superior olivary complex: medial and lateral superior olive. *Hearing Research*, 225(1-2):80–90.

- Kuwabara, N. and Zook, J. (1992). Projections to the medial superior olive from the medial and lateral nuclei of the trapezoid body in rodents and bats. *The Journal of Comparative Neurology*, 324(4):522–538.
- Kuwabara, N. and Zook, J. M. (1999). Local collateral projections from the medial superior olive to the superior paraolivary nucleus in the gerbil. *Brain Research*, 846(1):59–71.
- Lang, S. B., Bonhoeffer, T., and Lohmann, C. (2006). Simultaneous imaging of morphological plasticity and calcium dynamics in dendrites. *Nature Protocols*, 1(4):1859–1864.
- Larkman, A. and Mason, A. (1990). Correlations between morphology and electrophysiology of pyramidal neurons in slices of rat visual cortex. I. Establishment of cell classes. *The Journal of Neuroscience*, 10(5):1407–1414.
- MacLeod, K. M., Soares, D., and Carr, C. E. (2006). Interaural timing difference circuits in the auditory brainstem of the emu (*Dromaius novaehollandiae*). *The Journal of Comparative Neurology*, 495(2):185–201.
- Magnusson, A. K., Kapfer, C., Grothe, B., and Koch, U. (2005). Maturation of glycinergic inhibition in the gerbil medial superior olive after hearing onset. *The Journal of Physiology*, 568(Pt 2):497–512.
- Maier, J. K., Kindermann, T., Grothe, B., and Klump, G. M. (2008). Effects of omnidirectional noise-exposure during hearing onset and age on auditory spatial resolution in the Mongolian gerbil (*Meriones unguiculatus*) – a behavioral approach. *Brain Research*, 1220:47–57.
- Mainen, Z. and Sejnowski, T. (1996). Influence of dendritic structure on firing pattern in model neocortical neurons. *Nature*, 382(6589):363–366.
- Mason, A. and Larkman, A. (1990). Correlations between morphology and electrophysiology of pyramidal neurons in slices of rat visual cortex. II. Electrophysiology. *The Journal of Neuroscience*, 10(5):1415–1428.

- Mathews, P. J., Jercog, P. E., Rinzel, J., Scott, L. L., and Golding, N. L. (2010). Control of submillisecond synaptic timing in binaural coincidence detectors by K(v)1 channels. *Nature Neuroscience*, 13(5):601–609.
- McAlpine, D. and Grothe, B. (2003). Sound localization and delay lines – do mammals fit the model? *Trends in Neurosciences*, 26(7):347–350.
- McAlpine, D., Jiang, D., and Palmer, A. R. (2001). A neural code for low-frequency sound localization in mammals. *Nature Neuroscience*, 4(4):396–401.
- Middlebrooks, J. C. and Green, D. M. (1991). Sound localization by human listeners. *Annual Review of Psychology*, 42:135–159.
- Moore, D. R. and Kitzes, L. M. (1985). Projections from the cochlear nucleus to the inferior colliculus in normal and neonatally cochlea-ablated gerbils. *The Journal of Comparative Neurology*, 240(2):180–95.
- Moore, D. R., Schnupp, J. W. H., and King, A. J. (2001). Coding the temporal structure of sounds in auditory cortex. *Nature Neuroscience*, 4(11):1055–1056.
- Nevian, T. and Helmchen, F. (2007). Calcium indicator loading of neurons using single-cell electroporation. *Pflügers Archiv : European Journal of Physiology*, 454(4):675–688.
- Nordeen, K. W., Killackey, H. P., and Kitzes, L. M. (1983). Ascending auditory projections to the inferior colliculus in the adult gerbil, *Meriones unguiculatus*. *The Journal of Comparative Neurology*, 214(2):131–143.
- Overholt, E., Rubel, E., and Hyson, R. (1992). A circuit for coding interaural time differences in the chick brainstem. *The Journal of Neuroscience*, 12(5):1698–1708.
- Pecka, M., Brand, A., Behrend, O., and Grothe, B. (2008). Interaural time difference processing in the mammalian medial superior olive: the role of glycinergic inhibition. *The Journal of Neuroscience*, 28(27):6914–6925.

- Pecka, M., Zahn, T. P., Saunier-Rebori, B., Siveke, I., Felmy, F., Wiegrebe, L., Klug, A., Pollak, G. D., and Grothe, B. (2007). Inhibiting the inhibition: a neuronal network for sound localization in reverberant environments. *The Journal of Neuroscience*, 27(7):1782–1790.
- Rall, W. (1959). Branching dendritic trees and motoneuron membrane resistivity. *Experimental Neurology*, 1(5):491–527.
- Rall, W. (1960). Membrane potential transients and membrane time constant of motoneurons. *Experimental Neurology*, 2(5):503–532.
- Rall, W. (1964). Theoretical significance of dendritic trees for neuronal input-output relations. *Neural Theory and Modeling*, pages 73–97.
- Rall, W. (1969). Time constants and electrotonic length of membrane cylinders and neurons. *Biophysical Journal*, 9(12):1483–1508.
- Rall, W. (1995). Perspective on neuron model complexity. *Handbook of Brain Theory and Neural Networks*, pages 728–732.
- Rall, W., Burke, R., Holmes, W., Jack, J., Redman, S., and Segev, I. (1992). Matching dendritic neuron models to experimental data. *Physiological Reviews*, 72(4 Suppl):S159–S186.
- Rautenberg, P. L., Grothe, B., and Felmy, F. (2009). Quantification of the three-dimensional morphology of coincidence detector neurons in the Medial Superior Olive of gerbils during late postnatal development. *The Journal of Comparative Neurology*, 517(3):385–396.
- Rayleigh, L. (1876). On our perception of the direction of a source of sound. *Proceedings of the Musical Association*, 2:75–84.
- Rayleigh, L. (1907). On the dynamical theory of gratings. *Proceedings of the Royal Society of London. Series A, Containing Papers of a Mathematical and Physical Character*, 79(532):399–416.

- Reed, M. C., Blum, J. J., and Mitchell, C. C. (2002). Precision of neural timing: effects of convergence and time-windowing. *Journal of Computational Neuroscience*, 13(1):35–47.
- Rietzel, H. J. and Friauf, E. (1998). Neuron types in the rat lateral superior olive and developmental changes in the complexity of their dendritic arbors. *The Journal of Comparative Neurology*, 390(1):20–40.
- Rogowski, B. and Feng, A. (1981). Normal postnatal development of medial superior olivary neurons in the albino rat: a Golgi and Nissl study. *The Journal of Comparative Neurology*, 196(1):85–97.
- Rothman, J. S. and Manis, P. B. (2003). The roles potassium currents play in regulating the electrical activity of ventral cochlear nucleus neurons. *Journal of Neurophysiology*, 89(6):3097–3113.
- Rothman, J. S. and Young, E. D. (1996). Enhancement of neural synchronization in computational models of ventral cochlear nucleus bushy cells. *Auditory Neuroscience*, 2:47–62.
- Ryan, A. F., Woolf, N. K., and Sharp, F. R. (1982). Functional ontogeny in the central auditory pathway of the Mongolian gerbil. A 2-deoxyglucose study. *Experimental Brain Research*, 47(3):428–436.
- Ryugo, D. K. and Parks, T. N. (2003). Primary innervation of the avian and mammalian cochlear nucleus. *Brain Research Bulletin*, 60(5-6):435–456.
- Sanes, D. H., Goldstein, N. A., Ostad, M., and Hillman, D. E. (1990). Dendritic morphology of central auditory neurons correlates with their tonotopic position. *The Journal of Comparative Neurology*, 294(3):443–454.
- Sanes, D. H., Markowitz, S., Bernstein, J., and Wardlow, J. (1992a). The influence of inhibitory afferents on the development of postsynaptic dendritic arbors. *The Journal of Comparative Neurology*, 321(4):637–644.

- Sanes, D. H., Song, J., and Tyson, J. (1992b). Refinement of dendritic arbors along the tonotopic axis of the gerbil lateral superior olive. *Developmental Brain Research*, 67(1):47–55.
- Schaefer, A. T., Larkum, M. E., Sakmann, B., and Roth, A. (2003). Coincidence detection in pyramidal neurons is tuned by their dendritic branching pattern. *Journal of neurophysiology*, 89(6):3143–54.
- Schmitt, S., Evers, J. F., Duch, C., Scholz, M., and Obermayer, K. (2004). New methods for the computer-assisted 3-D reconstruction of neurons from confocal image stacks. *Neuroimage*, 23(4):1283–1298.
- Scott, L. L., Mathews, P. J., and Golding, N. L. (2005). Posthearing developmental refinement of temporal processing in principal neurons of the medial superior olive. *The Journal of Neuroscience*, 25(35):7887–7895.
- Seidl, A. and Grothe, B. (2005). Development of sound localization mechanisms in the mongolian gerbil is shaped by early acoustic experience. *Journal of Neurophysiology*, 94(2):1028–1036.
- Shneiderman, a., Oliver, D. L., and Henkel, C. K. (1988). Connections of the dorsal nucleus of the lateral lemniscus: an inhibitory parallel pathway in the ascending auditory system? *The Journal of Comparative Neurology*, 276(2):188–208.
- Smith, D. and Kraus, N. (1987). Postnatal development of the auditory brainstem response (ABR) in the unanesthetized gerbil. *Hearing Research*, 27(2):157–164.
- Smith, P., Joris, P. X., Carney, L., and Yin, T. (1991). Projections of physiologically characterized globular bushy cell axons from the cochlear nucleus of the cat. *The Journal of Comparative Neurology*, 304(3):387–407.
- Smith, P. H. (1995). Structural and functional differences distinguish principal from nonprincipal cells in the guinea pig MSO slice. *Journal of Neurophysiology*, 73(4):1653–1667.

- Smith, P. H., Joris, P. X., and Yin, T. C. (1993). Projections of physiologically characterized spherical bushy cell axons from the cochlear nucleus of the cat: evidence for delay lines to the medial superior olive. *The Journal of Comparative Neurology*, 331(2):245–260.
- Smith, Z. D. (1981). Organization and development of brain stem auditory nuclei of the chicken: dendritic development in N. laminaris. *The Journal of Comparative Neurology*, 203(3):309–333.
- Stiefel, K. and Sejnowski, T. (2007). Mapping function onto neuronal morphology. *Journal of Neurophysiology*, 98(1):513–526.
- Stotler, W. (1953). An experimental study of the cells and connections of the superior olivary complex of the cat. *The Journal of Comparative Neurology*, 98(3):401–431.
- Svirskis, G. and Rinzel, J. (2000). Influence of temporal correlation of synaptic input on the rate and variability of firing in neurons. *Biophysical Journal*, 79(2):629–637.
- Thompson, S. P. (1882). On the function of the two ears in the perception of space. *Philosophical Magazine*, 13:406–416.
- Tobin, A.-E., Van Hooser, S. D., and Calabrese, R. L. (2006). Creation and reduction of a morphologically detailed model of a leech heart interneuron. *Journal of Neurophysiology*, 96(4):2107–2120.
- Trussell, L. O. (1999). Synaptic mechanisms for coding timing in auditory neurons. *Annual Review of Psychology*, 61(1):477–496.
- Vetter, P., Roth, A., and Häusser, M. (2001). Propagation of action potentials in dendrites depends on dendritic morphology. *Journal of Neurophysiology*, 85(2):926–937.
- Wang, Y. and Rubel, E. W. (2008). Rapid regulation of microtubule-associated protein 2 in dendrites of nucleus laminaris of the chick following deprivation of afferent activity. *Neuroscience*, 154(1):381–389.

- Werthat, F., Alexandrova, O., Grothe, B., and Koch, U. (2008). Experience-dependent refinement of the inhibitory axons projecting to the medial superior olive. *Developmental Neurobiology*, 68(13):1454–1462.
- Wightman, F. L. and Kistler, D. J. (1992). The dominant role of low-frequency interaural time differences in sound localization. *The Journal of the Acoustical Society of America*, 91(3):1648–1661.
- Yin, T. C. and Chan, J. C. (1990). Interaural time sensitivity in medial superior olive of cat. *Journal of Neurophysiology*, 64(2):465–488.
- Zhou, Y., Carney, L. H., and Colburn, H. S. (2005). A model for interaural time difference sensitivity in the medial superior olive: interaction of excitatory and inhibitory synaptic inputs, channel dynamics, and cellular morphology. *The Journal of Neuroscience*, 25(12):3046–3058.

Epilogue

Linguistic Usage

Throughout my thesis I tried to apply the American variant of English. e.g. *modeling* instead of *modelling*. In the same line, I used the *serial comma* (e.g. *Pippi, Berta, and Paula*).

Instead of having a glossary, I decided to introduce abbreviations anew in every chapter and caption, respectively.

Computational setup

Most of the results and figures discussed in this thesis can be implemented, simulated, and visualized with regular personal computers. The following software was mainly used (from simple computations all the way to the typesetting of this thesis): *Amira*, *gimp*, *inkscape*, *KOMA-Script*, *L^AT_EX 2_ε*, *Linux*, *Matlab*, *matplotlib*, *NEURON*, *numpy*, *PostgreSQL*, *python*, *scipy*, *SQLAlchemy*, *SQLite*, *vim*, *xpp*

Danksagung

Zuerst möchte ich mich bei Felix bedanken, der sich ohne Zögern darauf eingelassen hat, mich bei meiner interdisziplinären Doktorarbeit zu betreuen. Er führte mich in die Kunst des Experimentierens ein und zeigte mir zusammen mit Olga, wie die Neurone mit Hilfe eines konfokalen Mikroskops in einen dreidimensionalen Bilderstapel verwandelt werden konnten. Olga, an dieser Stelle auch ein herzliches Dankeschön

an Dich für die Geduld trotz des ungemütlichen und kalten Konfokalmikroskopier-aumes.

Vielen Dank auch an Dich, Christian, für Deine Betreuung und Unterstützung beim theoretischen Teil meiner Arbeit. Ein knappes Jahr bist Du fast ohne Unterbrechung einmal pro Woche mit mir meine aktuellen Ergebnisse durchgegangen. Gerade während der Zeit meiner beruflichen Doppelbelastung war mir Dein regelmäßiger Rat der notwendige Leitfaden für das Anfertigen dieser vorliegenden Arbeit.

Das Ganze wurde erst durch Dich, Benedikt, ermöglicht. Du hast mir bei meiner anfänglichen Suche nach einem passenden Thema die Herausforderung anvertraut, für die MSO ein Multikompartiment-Modell zu entwickeln. Während meiner gesamten Zeit am Institut warst Du immer im richtigen Moment präsent. Vielen Dank für Deine stete Unterstützung!

Der gute Kontakt zum MPI für Neurobiologie hat mir anfänglich enorm geholfen, mich in meinen neuen, theoretischen Methoden zurechtzufinden. Axel, Du hast den Kontakt hergestellt, insbesondere zu Franz, Friedrich und Hubert. Wir haben uns über zweieinhalb Jahr¹ regelmäßig getroffen und Methoden theoretischer Neurowissenschaften diskutiert und schließlich unseren Buchklub gegründet. Obwohl alle Beteiligten stark in das Tagesgeschäft eingespannt waren, hat sich jeder einzelne trotzdem für diese Treffen Zeit genommen und sich zum Teil sogar intensiv darauf vorbereitet! Euch allen *von drüben* vielen Dank dafür.

Nicht zu vergessen, meine Bürokollegen Marc und Gonzalo. Mit Euch konnte ich allzeit vortrefflich über das Zusammenspiel von Modell und Experiment diskutieren. Ob es geholfen hat? Siehe Kapitel ein bis sechs!

Mein spezieller und besonderer Dank gilt meinen colegas Álvaro, Hannes² und Michael. Ihr wart immer meine Anlaufstelle, sei es, dass irgendwo der Schuh gedrückt hat, oder dass ich eine unglaubliche Erkenntnis hatte³, die sofort mitgeteilt wer-

¹Ja, tatsächlich zweieinhalb Jahre! Ich habe ein wenig recherchiert: von Herbst 2006 bis Sommer 2008.

²Hannes, ohne unser 50 l Bierfassabkommen würde ich wohl immernoch schreiben – ich freue mich schon auf die Feier!

³Wenigstens für diesen Augenblick...

den musste. Unvergesslich bleibt unser legendäres, internes Seminar (ich sag nur *Breiman*) in Verbindung mit unseren philosophisch-statistischen Mittagspausenspaziergängen – ohne jegliche Denkkonventionen, immer bemüht über rein methodische Aspekte hinauszublicken.

Eine Peron darf an dieser Stelle nicht fehlen: Katharina, Du hast mir nicht zuletzt bei meinem (zweijährigen) Endspurt immer den Rücken frei gehalten und mich unterstützt, wo immer Du konntest. Vielen Dank aus ganzem Herzen an Dich!